AD-A037 836 MASSACHUSETTS INST OF TECH CAMBRIDGE AEROPHYSICS LAB F/G 20/4
WAKE MEASUREMENTS BEHIND A MAGNETICALLY-SUSPENDED SPINNING AND --ETC(U)
FEB 77 D M FINN, C W HALDEMAN, E E COVERT DAAD05-74-C-0735
UNCLASSIFIED TR-195 BRL-CR-331 NL

1 OF 1
ADA037836

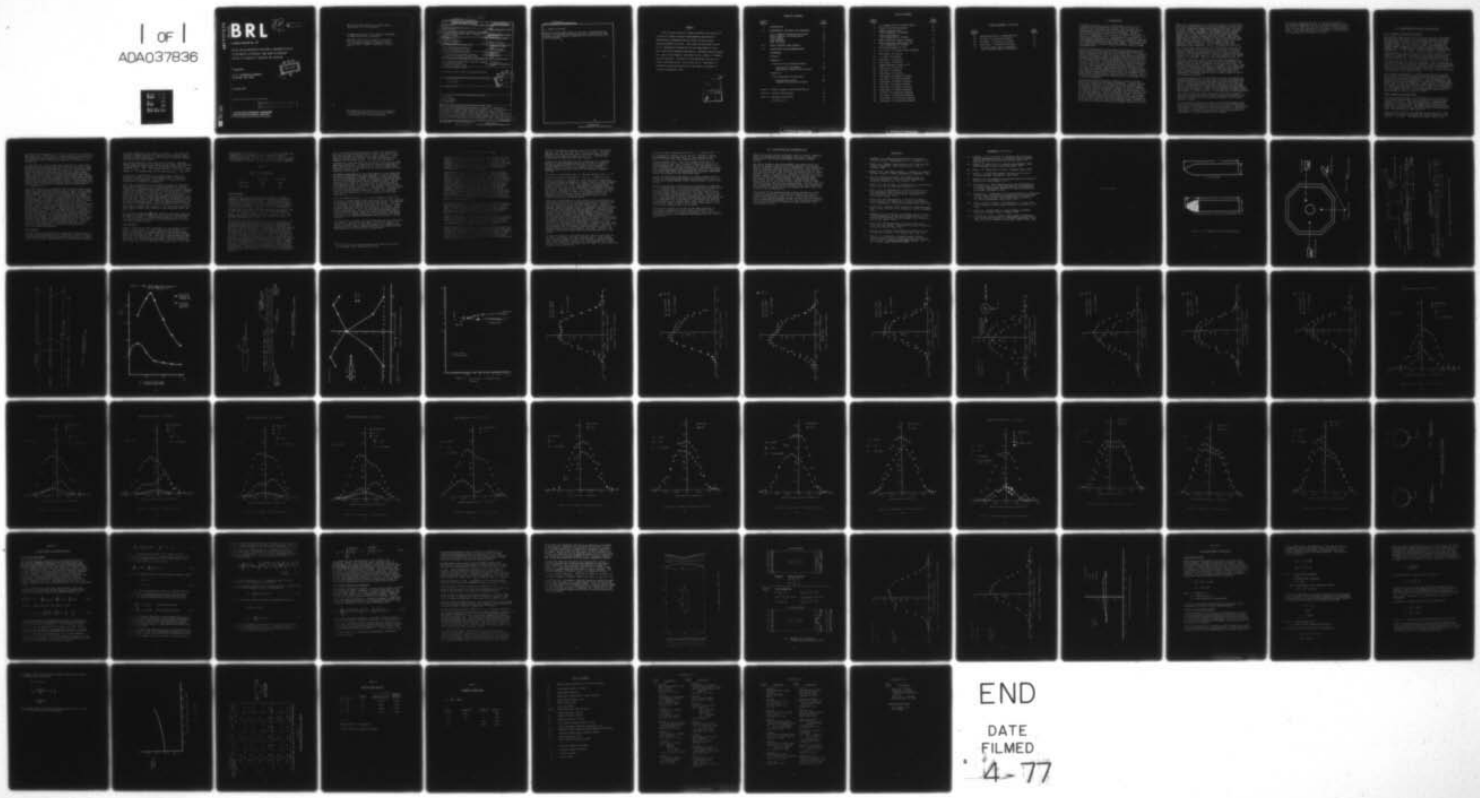

END

DATE FILMED
4-77

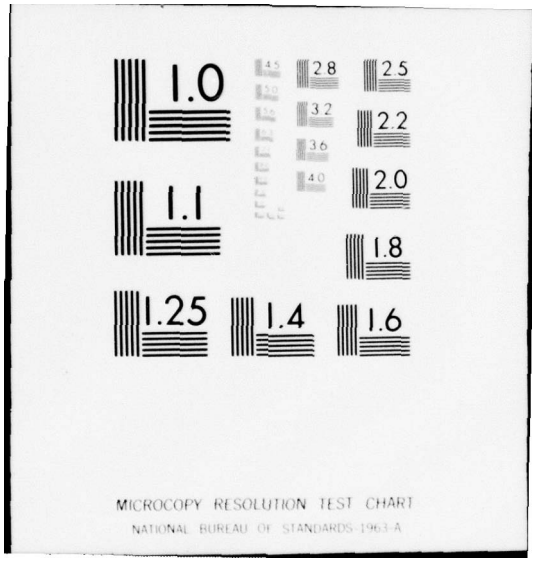
1.0
1.1
1.25
1.4
1.6
1.8
2.0
2.2
2.5
2.8
3.2
3.6
4.0
4.5
5.0
MICROCOPY RESOLUTION TEST CHART
NATIONAL BUREAU OF STANDARDS-1963-A

BRL CR 331

BRL

12 pp

AD

CONTRACT REPORT NO. 331

WAKE MEASUREMENTS BEHIND A MAGNETICALLY-SUSPENDED SPINNING AND NON-SPINNING OGIVE CYLINDER AT ANGLES OF ATTACK

Prepared by

M. I. T. Aerophysics Laboratory
Cambridge, MA 02139

February 1977

USA BALLISTIC RESEARCH LABORATORY
ABERDEEN PROVING GROUND, MARYLAND

Destroy this report when it is no longer needed.
Do not return it to the originator.

Secondary distribution of this report by originating or sponsoring activity is prohibited.

Additional copies of this report may be obtained from the National Technical Information Service, U.S. Department of Commerce, Springfield, Virginia 22151.

The findings in this report are not to be construed as an official Department of the Army position, unless so designated by other authorized documents.

UNCLASSIFIED

SECURITY CLASSIFICATION OF THIS PAGE (When Data Entered)

REPORT DOCUMENTATION PAGE

READ INSTRUCTIONS BEFORE COMPLETING FORM

1. REPORT NUMBER: BRL Contract Report No. 331	2. GOVT ACCESSION NO.
3. RECIPIENT'S CATALOG NUMBER	
4. TITLE (and Subtitle): WAKE MEASUREMENTS BEHIND A MAGNETICALLY-SUSPENDED SPINNING AND NON-SPINNING OGIVE CYLINDER AT ANGLES OF ATTACK.	5. TYPE OF REPORT & PERIOD COVERED: Final rept.
	6. PERFORMING ORG. REPORT NUMBER: MIT TR-195
7. AUTHOR(s): Douglas M. Finn, Charles W. Haldeman, Eugene E. Covert	8. CONTRACT OR GRANT NUMBER(s): DAAD05-74-C-0735
9. PERFORMING ORGANIZATION NAME AND ADDRESS: M.I.T. Aerophysics Laboratory, Cambridge, Massachusetts 02139	10. PROGRAM ELEMENT, PROJECT, TASK AREA & WORK UNIT NUMBERS: RDT&E 1L161102AH43
11. CONTROLLING OFFICE NAME AND ADDRESS: U.S. Army Ballistic Research Laboratory, Aberdeen Proving Ground, Maryland 21005	12. REPORT DATE: FEBRUARY 1977
	13. NUMBER OF PAGES: 79
14. MONITORING AGENCY NAME & ADDRESS (if different from Controlling Office): U.S. Army Materiel Development & Readiness Command, 5001 Eisenhower Avenue, Alexandria, Virginia 22333	15. SECURITY CLASS. (of this report): Unclassified
	15a. DECLASSIFICATION/DOWNGRADING SCHEDULE

16. DISTRIBUTION STATEMENT (of this Report)

Approved for public release; distribution unlimited.

17. DISTRIBUTION STATEMENT (of the abstract entered in Block 20, if different from Report)

75 p.

DDC RECEIVED APR 6

18. SUPPLEMENTARY NOTES

19. KEY WORDS (Continue on reverse side if necessary and identify by block number)

Magnus Force
Magnetic Balance
Wake Measurements
Subsonic Flow

20. ABSTRACT (Continue on reverse side if necessary and identify by block number) (lcb)

Total pressure measurements were performed in the wake of a magnetically-suspended ogive nosed cylinder immersed in a subsonic flow. Profile drag was computed by the momentum defect method and compared to magnetic balance measurements. Impact pressure wake profiles were then recorded to investigate the effects of varying Reynolds number, angle of attack, spin rate, and transition on wake characteristics. Fully turbulent boundary layer conditions served to attenuate this reverse Magnus force and promote a linear relationship → next page (Continued)

DD FORM 1 JAN 73 1473 EDITION OF 1 NOV 65 IS OBSOLETE

009200

UNCLASSIFIED

SECURITY CLASSIFICATION OF THIS PAGE (When Data Entered)

20. ABSTRACT (Continued):

between the induced sidewash angle and spin rate. Interpretation of the pressure surveys enabled a qualitative assessment of flow conditions about the body to be made, leading to suggestions as to a possible source of the observed phenomena.

PREFACE

This Interim Scientific Report presents the results of a series of impact pressure measurements made behind a magnetically-suspended spinning ogive cylinder under Contract DAAD05-74-C-0735. This work was performed at the M.I.T. Aerophysics Laboratory for the Department of the Army, Ballistics Research Laboratory, Aberdeen Proving Ground, Md., under the technical cognizance of Mr. Anders S. Platou, Contract Monitor. The bulk of this material was part of a thesis submitted by Mr. Finn to the M.I.T. Department of Aeronautics and Astronautics for the degree of Master of Science in February, 1976.

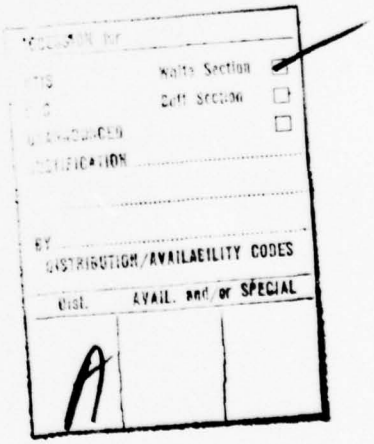

TABLE OF CONTENTS

LIST OF FIGURES

LIST OF FIGURES (continued)

I. INTRODUCTION

Although the effects of spin-induced Magnus force on the trajectories of axisymmetric projectiles were first observed in the mid-nineteenth century, both theoretical and experimental research in the field continues. The discovery and classical explanation of the Magnus effect has been well documented in such reviews as those of Jacobson (1), Platou (2) and Swanson (3). Experimentation performed on large aspect ratio spinning cylinders in a crossflow indicates a non-linear dependance of the spin-induced force on spin rate not predicted by the two-dimensional theory. Transition has also been shown to grossly affect the Magnus force in these experiments (4).

Extensive theoretical and experimental consideration of the Magnus effect has been applied to gyroscopically stabilized spinning projectiles since the end of World War II. A spinning body of revolution at angle of attack experiences potentially destabilizing Magnus forces and moments generated by the spin-induced pressure difference on opposing sides of the body in the crossflow plane. The preponderance of analytical work has focused on the case of attached flow under varying conditions of spin, angle of attack, Reynolds and Mach numbers. Recent work (5), for example, predicts Magnus force and moment coefficients for laminar compressible flow about several typical body geometries by considering two sources of the Magnus effect, these being circumferential distortion of the boundary layer displacement thickness due to spin and angle of attack, and the variation of radial pressure gradient due to centrifugal forces at the circumference.

Experimental efforts generally encounter several problems which are inherent in the Magnus phenomenon. Delicate dynamic balancing of the model is required to reduce resonant speed oscillations owing to an off-axis center of gravity location. In addition, forces and moments measured in the yaw plane are at least an order of magnitude less than the body normal forces and pitching moments. Thus, high sensitivity and repeatability must be designed into the data recording system. As a result of the required strain gauge sensitivity and the substantial boundary layer transition effect on Magnus forces and moments, wind tunnels chosen for such investigations should possess low levels of free stream turbulence and dynamic pressure variation.

Smoke flow visualization (6,7) has been useful in delineating the basic interaction of the problem parameters of spin, angle of attack, Reynold's number and transition effects. At small angles of attack, low energy lift-induced lee side vorticity is shown to remain embedded in the boundary layer, thereby distorting it. For flows of sufficiently small Reynolds number, spin induces a skewed laminar boundary layer which presents an effectively asymmetric body to the oncoming flow. Under laminar, zero spin conditions, higher angles of attack cause two vortex sheets to separate symmetrically from opposite sides of the body. At low values of the non-dimensional spin parameter, $PD/2V_\infty$, the resultant motion of the vortex whose rotation vector is aligned with that of the body is away from the surface, while the vortex of opposite rotation remains in close proximity to the body and is displaced in the direction of spin. However, flow visualization reveals that for high values of the spin parameter, the vortex geometry is reversed. That is, with increasing $PD/2V_\infty$, the left-hand (aligned) vortex is seen to lose its identity in moving closer to the body surface while the right-hand vortex remains distinct and is displaced in the spin direction. It has been suggested in Jacobson's (1) review on the subject that transition from laminar to turbulent boundary layer conditions is the most important flow condition about spinning shells; this is based on spark photography (8) results showing an asymmetric transition line on a cone at small angle of attack in a supersonic stream.

Recent measurements (9) of the Magnus force on a magnetically-suspended spinning five caliber ogive cylinder have shown that a sign reversal occurs for small angles of attack around 2 degrees. Increasing Reynold's number, addition of trip devices and the introduction of "dummy" sting apparatus into the base flow region all served to attenuate the observed reversal effect and tended to promote a linear relation between the Magnus force coefficient, C_Y, and spin rate. To explain this it was postulated that body vortices in close proximity to the model cause an altered pressure distribution which contribute a dominant force opposite in direction to the classical Magnus force at small angles of attack.

In the present investigation impact pressure measurements were made in the wake behind a spinning ogive cylinder magnetically suspended in a low turbulence subsonic wind tunnel. Interference-free support of the model in this facility offers an excellent opportunity to study the wake characteristics corresponding to the positive and negative Magnus force regimes.

To provide a comparative check of the drag force and corresponding momentum defect, the momentum defect method due to B. M. Jones (10) is then applied to calculate profile drag from one wake velocity profile behind a non-spinning model. The drag coefficient so calculated is then compared to force data from the magnetic balance.

II. EXPERIMENTAL APPARATUS AND PROCEDURE

M.I.T. Magnetic Balance Wind Tunnel

The subsonic wind tunnel used in conjunction with the magnetic balance system at the M.I.T. Aerophysics Laboratory provides low turbulence flow and sting-free support of the 5:1 ogive cylinder model. The open circuit tunnel has a maximum flow Reynolds number of five million per foot, corresponding to a peak dynamic pressure of 2.6 lb/in^2 for zero blockage conditions (11). A free stream turbulence level of .26% has been measured for V_∞ = 300 ft/sec. Dynamic pressure decreases longitudinally in the test section by 2% from entrance to exit. A horizontal buoyancy correction is therefore needed, as detailed in Appendix B. Transverse dynamic pressure variation does not exceed ± .2% q_∞ for distances greater than or equal to one inch from the test section boundaries. The test section is a closed octagonal jet made of plexiglass, with a cross-section area of 32.63 in^2 at the model location. The pressure difference from two static taps on the tunnel contractor is calibrated versus test section dynamic pressure providing a means of setting flow velocity at the desired level.

All pressure measurements, including speed setting, are made with a 100 torr full-scale MKS Baratron pressure transducer. The repeatability and uncertainty for this instrument are .005 mm Hg and ± .001 mm Hg respectively. The time response of the pressure system was studied and it was found to be sufficiently short that it could be neglected. Model support in five degrees of freedom and spin about the horizontal axis is accomplished with the magnetic balance system (12). Model roll is generated by a two phase, 1200 Hz A.C. electromagnetic field which is superimposed on the D.C. support fields.

Model Geometry and Positioning

The wake pressure surveys are performed in the flow behind a five caliber tangent-ogive nose projectile of one inch base diameter (Figure 1). The one-pound model is machined from electrolytic ingot iron and is plated with a copper layer nominally .003 inch thick. The copper plating is used to improve model response to the position sensor, decrease system noise and improve spin field coupling.

Black and white striping was applied to the tail end of the afterbody to trigger a photocell and transit focused on this portion of the body. The amplified output signal of the

photocell was connected to two digital counters for monitoring model spin rate. When desired, forced boundary layer transition was induced by the application of #180 carborundum grit in a one-inch wide strip, beginning one-quarter inch from the nose (Figure 1b).

In past work (9) a thin center body supported by piano wires extending through the diffuser walls served to position dummy stings at a fixed distance behind a similar five-caliber model. This stationary body was used to support the impact probe to avoid the blocking associated with a movable pylon mounted probe. All survey data in the wake was therefore obtained by translation of the model in front of this fixed probe. Because Magnus force acts in the horizontal plane, most traverses were made moving the model horizontally in slip. Unfortunately, this model motion prohibits use of the helium neon laser positioning system, which is capable of reducing angular uncertainty to ± .02 degrees (13).

Surveying transits were therefore used to monitor model translation and angulation by aligning the crosshairs with an edge or other straight line feature of the model. Three transits were used to monitor model position in five degrees of freedom (Figure 2). Lift and drag are concentrated in one instrument. A second transit is aimed at a mirror under the test section which reflects slip and yaw information. Pitch alone is viewed through the last transit. With the crosshairs serving as reference lines, the model is brought into position by adjusting the D.C. level fed into the balance positioning system from external position command boxes. Model position uncertainty using the transits is ± .001 inch in translation and ± .1 degree in angular displacement. It is felt that these uncertainties are reliable for all angles of attack in the present investigation except zero degrees. For the case where the model is non-spinning and aligned, or closely aligned with the flow, unsteady boundary layer effects on alternating sides of the model base seem to be the cause of observed jittery behavior. In this case, position uncertainty is estimated from the transit operators' experience as ± .030 inch in translation and ± .2 degrees in angular displacement.

Probe Design

An impact probe was designed for minimum flow disturbance and minimal flow misalignment error. This probe, shown in Figure 3, is constructed of #17 gauge hypodermic tubing with a drilled-out brass insert forming the probe tip. The probe support assembly

is shown installed in the tunnel in Figure 4. The probe and the brass sleeve retaining it comprise a sufficiently small volume of conductive material that effects on magnetic balance performance are undetectable.

The characteristics of the probe are as follows. Reynolds number based on sensing hole radius at the lowest test velocity is approximately 500; therefore, viscosity effects may be neglected ($Re_a > 100$). The recovery factor is 100% for a Mach number of .25 corresponding to the high test $Re_L = 7.50 \times 10^5$.

An effective displacement of the probe center occurs for measurements made in a velocity gradient such as occurs in boundary layers and wakes. This effect is discussed and a correction is computed in Appendix B.

The probe is positioned in the tunnel by adjusting the piano wire support tension (Figure 4) while focusing the various transits on a removable probe sheath which slips over the brass sleeve and extends into the center of the test section. The extension was necessary, since the coils of the magnetic balance block the view of probe tip position. The probe tip was arbitrarily located 3.0 model base diameters downstream of the trailing edge. This position was chosen in an attempt to have the probe near enough to the model for good sensitivity but out of the recirculation region. Static pressure measurements in the wake of an axisymmetric blunt based model at $Re_L = 118{,}000$ were made by Kangovi (14), Figure 5. He found that wake centerline static pressure had returned to the freestream value for $X/D = 3.0$.

At this axial probe tip position, however, the model could not be raised high enough to measure wake centerline properties at 7^o angle of attack. A kinked probe (Figure 3) with the same tip properties but with the tip offset downward was utilized for high incidence testing.

Test Schedule

Table A indicates the test conditions for the present investigation. Pitch angles of 2 and 7 degrees were chosen as a result of previous force measurements (9), which show these model inclinations to produce side force coefficients of equal magnitude but opposite sign. Reference 9 also determined that tests run at a flow speed of 300 ft/sec exhibited significant non-linear and reversal characteristics. Test velocities of 282 ft/sec ($Re_L = 7.50 \times 10^5$) and 119 ft/sec ($Re_L = 3.15 \times 10^5$)

were chosen to illustrate the effect of Reynolds number and transition on the Magnus effect. This combination of Reynolds number and reduced spin is shown in Table I. The range of spin rates was chosen to utilize the full capability of the magnetic balance for this particular model geometry.

Table I

$\frac{PD}{2V}$ for Run Conditions

Re	3.15×10^5	7.5×10^5
Low Spin	.154	.065
High Spin	.330	.139

Test Procedure

During testing the data was taken as follows. Ambient pressure, temperature and relative humidity were recorded before and after each set of runs. Impact pressure was measured as a pressure difference from atmospheric pressure using the MKS Baratron. For loss-less flow in the tunnel, the pressure difference $(p_{at}-p_o)$ is zero. The extent of pressure loss was measured before and after each set of runs by recording $(p_{at}-p_o)_{tare}$ at the test velocity without a model. In addition, static pressure as detected by a test section wall tap in the plane of the probe tip (Figure 4) was also recorded at this time.

After taking the tare readings the model was inserted in the balance, its pitch angle and spin rate were approximately set and the wind was brought up to speed by measuring the contractor static tap pressure difference. Model spin during testing was held to within ± 3% of the specified spin rate. With the model on the tunnel vertical centerline and its pitch and spin set for the test, lift position was adjusted to obtain the peak pressure defect. Thus, all traverses in slip were obtained on or near the vertical wake centerline. Clearly, spin induced sidewash prevents the exact lift centerline position from being located using this method. Since true wake characteristics for any particular test configuration are not known a priori, this method of traversing the thickest part of the wake was considered the most practical and expedient. Additional lift traverses were also performed one-half inch above and below the lift centerline position (Table A).

After lift position was adjusted the model was translated in the negative slip direction (Table A) until the edge of the wake was detected, as indicated by impact pressure, or until magnetic support was degraded. The wake traverse was then conducted by recording $(p_{at}-p_o)$ in 1/16 inch increments, progressing in the positive slip direction* until the far wake edge was encountered. Checkpoints to determine repeatability were taken in the viscous shear layer, where readings were generally stable, in the wake core and at zero tunnel vertical centerline displacement.

In previous experiments in this wind tunnel, slight pitch and yaw flow inclinations have been detected. Prior to execution of the test schedule an attempt was made to remove any existing flow misalignment relative to the model by adjusting pitch and yaw so as to produce an axially symmetric wake. Coarse traverses were taken in lift and slip for various angles of misalignment (Figure 7) to predict the correct model orientation relative to the transits for flow symmetry. The correction to pitch was determined to be - .2 degrees and .13 degrees for yaw (nose rotated counterclockwise). Thus, all effective pitch and yaw angles (α_e, β_e) are referenced to this model orientation.

Prior to taking data at α_e = 0, 2 and 7 degrees, either the straight or kinked impact probe was positioned with the transits, as discussed in the section entitled Probe Design. Uncertainty of the probe tip in both slip and lift was within ± .19 inch, corresponding to an angular uncertainty of 1.0 degree. Probe position remained fixed for all runs after the initial probe transit positioning. Zero spin profiles in Figures 9 and 12 show offsets not greater than the above-mentioned uncertainty relative to the tunnel centerline, and are used as the datum wake position in deducing subsequent spin and angle of attack effects.

The implication is that individual wake profiles are internally consistent. Indeed, one can compare effects of changes in angle of attack, spin or Reynolds number on the shape of the profiles but one cannot compare wake positions unless the data was collected at the same tunnel installation.

*N.B. positive slip direction places the probe to the right of the model when viewed from the rear.

III. TOTAL PRESSURE WAKE SURVEYS

The wake survey results are presented and discussed in this section in light of past Magnus work. In addition, the attenuation of these effects with the onset of the turbulent boundary layer condition is observed. In addition, the scale of pertinent wake characteristics is established so that probes designed for future flow angularity work may be optimized for minimal flow disturbance.

The boundary layer condition on the model can be deduced from the drag measurements of Figure 8. A laminar boundary layer on a clean model is exhibited by a decreasing drag coefficient up to a critical Reynolds number of approximately 100,000. Between 100,000 and 10^6 the clean model is transitional. Above 6×10^5 the tripped model appears to have a fully-developed turbulent boundary layer. Thus, boundary layer conditions for the low test flow velocity are fully laminar. The transitional Reynolds number flow regime represented by the high test flow velocity (282 ft/sec) is a favorable test condition due to the observed amplification of non-linear and reversal effects in past work. Also, the boundary layer on a roughened model is fully turbulent at Re_L = 750,000, thereby affording an evaluation of transition effects on wake properties.

It will be assumed for the test velocities considered that a turbulent wake exists. Certainly this is true for instances when the boundary layer is turbulent at the body trailing edge. Due to a velocity profile inflection point, however, the wake also tends to be turbulent even when a laminar boundary layer persists to the trailing edge (15).

Total pressure wake profiles detailing the effects of Reynolds number, spin, angle of attack and transition are presented in Figures 9 through 30. Maximum data point uncertainty was ± .1 mm Hg, while repeatability, although varying with test configuration, was generally better than .2 mm Hg.

Notice in particular Figures 17 through 21, which contain the offset velocity profile curves, for each particular test configuration, corresponding to the probe lift positions relative to the wake centerline. It will be recalled (Table A) that in addition to traverses performed on the wake horizontal centerline, data was also recorded for traverses one-half inch above and below this position.

Figure 31 represents a typical rear view of the flow at zero spin for low (2^{o}) and high (7^{o}) angle of attack. At small α embedded lee side vortices cause a thickened upper surface boundary layer while at larger values of α, a symmetrical vortex pair is shed from the upper surface.

Evidence of the separation of the vortex pair at 7 degrees appears in the bifurcated centerline profiles of Figure 9. No such distinct effects are noticed in the low angle of attack profiles of Figure 12, probably due to minimal boundary layer distortion from the low intensity embedded vortices.

The effect of increasing spin on the wake geometry for $\alpha_e = 7^{o}$ is seen in Figures 9 through 11. For $\alpha_e = 2$ degrees it is shown in Figures 17 through 19. This particular combination of Reynolds number and angle of attack, Figure 19, does generate distinct vortices of sufficient strength to be detected by the probe located at X/D = 3.0. The effect of decreased total pressure in the core and the subsequent displacement with spin are clearly observed in the + 1/2" curves of Figures 17 and 18. The profile amplitude is seen to be greatly enhanced and displaced at this higher spin rate, corroborating past flow visualization (6) studies and the boundary-layer vortex geometry hypothesis presented above.

Analytical considerations of the forces acting on slightly inclined spinning bodies of revolution have as yet failed to predict the occurrence of the reverse Magnus force. The most complete theory by Vaughn and Reis (5) applies to bodies with attached laminar boundary layers in supersonic flow and accounts for variable nose shape and compressibility. Included in the theory are the contributions to the Magnus force of distorted boundary layer thickness and radial pressure gradient in addition to empirical data on the effect of lee side vorticity. The findings assert that Magnus forces are directly proportional to boundary layer thickness and local body radius. Two explicit non-linear effects are also delineated. Firstly, lee side vorticity in the laminar attached flow is suggested as the cause of side force non-linearity with angle of attack. Secondly, the flow asymmetry due to boundary layer distortion accounts for observed Magnus force non-linearity with spin. However, the presence of explicit vortex pairs is not accounted for by the theory.

As angle of attack is increased the lee side vortices gain in strength, thickening the upper boundary layer. Sufficiently small Reynolds number and spin rate produce a laminar boundary layer which undergoes separation in the crossflow plane lower down on the cylindrical surface than for mixed or fully turbulent boundary layer conditions.

Profiles of wake characteristics for α_e = 7 degrees and P > 0 are presented in Figures 20, 21 and 22. Birtwell's force measurements for the same model (9) have indicated that at $Re_L = 7.7 \times 10^5$, this test configuration results in the classical Magnus force. The lift-induced vortex pair is clearly seen in the + 1/2" curves of Figures 21 and 22. The fully-developed spin effect is seen in the bifurcated profile of Figure 21. The left-hand peak is interpreted as being due to the diminished velocity associated with the reattached left-hand vortex while the separated and displaced right-hand vortex is reflected in the right-most peak.

Exactly the opposite distribution of vortex strength is observed in the low Reynolds number test condition of Figure 22, suggesting a marked change in the vortex boundary layer interaction.

Pressure measurement repeatability was degraded to a maximum of 1.5 mm Hg for the ± 1/2" profiles during gritted model tests. This is probably due to position uncertainty not $\Delta p/q$ uncertainty since changes in pressure are caused both by model position changes and unsteadiness in the flow. Turbulent mixing of the wake region and the adjoining laminar free stream flow can be expected to exhibit intermittent turbulent behavior. Thus, unsteadiness in the readings is attributed to inherent intermittency in the viscous shear layer rather than to gross motion of the wake. Figure 27 is a worst case example of the data scatter incurred due to this effect.

Referring to Figures 28, 29 and 30 the wake structure is essentially preserved with the onset of turbulent flow. Measured increases in C_Y due to turbulence, then, are due to enhancement of the flow asymmetry associated with the classical Magnus force.

IV. CONCLUSIONS AND RECOMMENDATIONS

Wake profiles for varying spin rate, angle of attack, Reynolds number and boundary layer conditions were shown to be consistent with the flow characteristics relevant to Magnus testing.

The impact pressure wake measurements have demonstrated the ability to discern the basic flow characteristics associated with an inclined, spinning body of revolution. Data acquisition could be improved with the insertion of an oscillator in the slip position control loop to obtain continuous plots of impact pressure versus slip position. Sweeping of the model in this manner, however, involves position control problems which could possibly lead to extensive redesign of the existing model positioning system. Alternatively, a movable probe design would allow use of the laser system, thereby improving model position control and wake data repeatability. Finally, hot wire three-dimensional flow angularity wake studies are recommended to elucidate the nature of the wake beyond the basic level presented in this investigation.

Application of the momentum defect method (Appendix A) using a radial distribution of wake impact pressure resulted in a predicted profile drag error of 5.3%. Free stream static pressure was assumed constant across the wake for this calculation. Subsequent measurement of the static pressure variation was shown to reduce the difference in the two profile drag calculations to 4.8%.

REFERENCES

1. Jacobson, I D, "Magnus Characteristics of Arbitrary Rotating Bodies", AGARDograph No. 171, November, 1973.

2. Platou, A S, "Magnus Characteristics of Finned and Non-finned Projectiles", AIAA Journal, Vol 3, No. 1, January, 1965.

3. Swanson, W H, "The Magnus Effect: A Summary of Investigations to Date", J Basic Engineering, September, 1961.

4. Kelly, H R and R W Van Aken, "The Magnus Force on Spinning Cylinders", Institute of the Aeronautical Sciences, Preprint No. 712, January, 1957.

5. Vaughn, H R and G E Reis, "A Magnus Theory", AIAA Journal, Vol 11, No. 10, pp 1396-1403, October, 1973.

6. Martin, J M, "An Experimental Correlation between the Flow and Magnus Characteristics of a Spinning Ogive-Nose Cylinder", Ph.D. Dissertation, University of Notre Dame, August, 1971.

7. Lando, D W, "An Investigation to Control the Magnus Characteristics of Symmetrical Fin and Nonfin Bodies", Ph.D. Dissertation, University of Notre Dame, May, 1972.

8. Sturek, W B, "Boundary Layer Studies on a Spinning Cone", AIAA Journal, Vol 10, No. 9, Paper No. 72-567, September, 1972.

9. Haldeman, C W, E P Birtwell, J B Coffin and E E Covert, "Some Measurements of the Magnus Characteristics on a Magnetically-Suspended Ogive-Cylinder", MIT Aerophysics Lab TR 193, April, 1976.

10. Jones, B M, "The Measurement of Profile Drag by the Pitot Traverse Method", Cambridge University Aeronautics Laboratory, ARL RM 1688, 1936.

11. Vlajinac, M, "Design, Construction and Evaluation of a Subsonic Wind Tunnel", S.M. Thesis, MIT, June, 1970.

12. Covert, E E, M Vlajinac, T Stephens and M Finston, "Magnetic Balance and Suspension Systems for Use with Wind Tunnels", Progress in Aerospace Science, Chapt II, 14, Pergamon Press, pp 27-107, 1973.

REFERENCES (continued)

13. Haldeman, C W, J B Coffin, E P Birtwell and M Vlajinac, "Magnus Measurements with the Magnetic Balance System", BRL CR 153, MIT Aerophysics Lab TR 187, May, 1974. (AD #782753)

14. Kangovi, S, "Base Flow of a Spinning Axisymmetric Body", AIAA Northeast Student Conference Paper, 1975.

15. Chang, P K, "Separation of Flow", Pergamon Press, 1966.

16. Taylor, G I, "The Determination of Drag by the Pitot-Traverse Method", ARC R&M No. 1808, 1937.

17. Hamming, R W, "Introduction to Applied Numerical Analysis", McGraw-Hill Book Company, 1971.

18. Silverstein, A, "Wake Characteristics and Determination of Profile Drag by the Momentum Method", Proceedings of the Fifth International Congress for Applied Mechanics, pp 403-405, September, 1938.

19. Zwaaneveld, J, "Comparison of Various Methods for Calculating Profile Drag from Pressure Measurements in the Near Wake at Subcritical Speeds", AGARD Conference Proceedings No. 124 on Aerodynamic Drag, April, 1973.

20. Young, A D and J N Maas, "The Behaviour of a Pitot Tube in a Transverse Total-Pressure Gradient", ARC RM No. 1770, 1936.

21. Gent, B L, "Interference in a Wind Tunnel of Regular Octagonal Section", ACA-2, January, 1944.

22. Silverstein, A and J A White, "Wind Tunnel Interference with Particular Reference to Off-Center Positions of the Wing and to the Downwash at the Tail", NACA R #547, 1935.

Figures

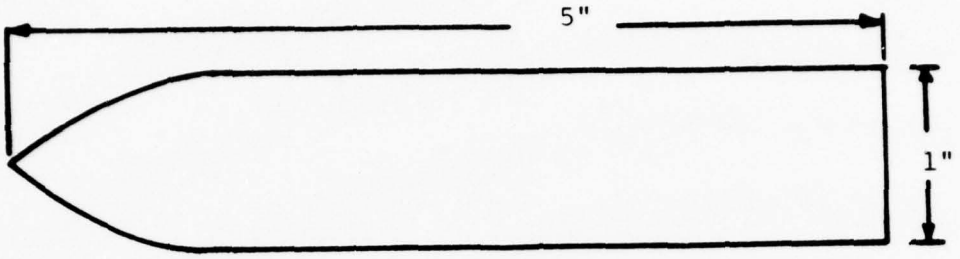

a) Bare Model

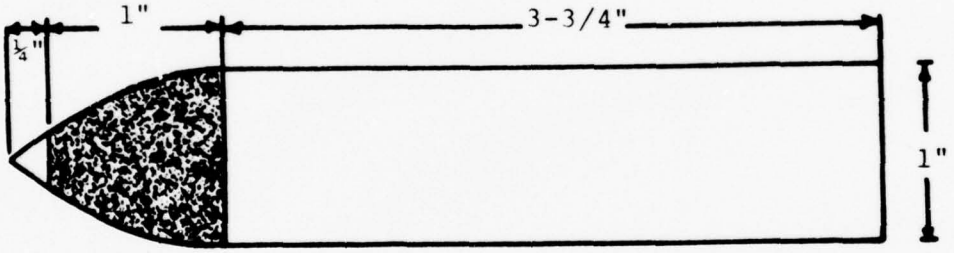

b) Tripped Model using #180 Carborundum Grit

Figure 1. 5:1 Tangent Ogive Cylinder Models

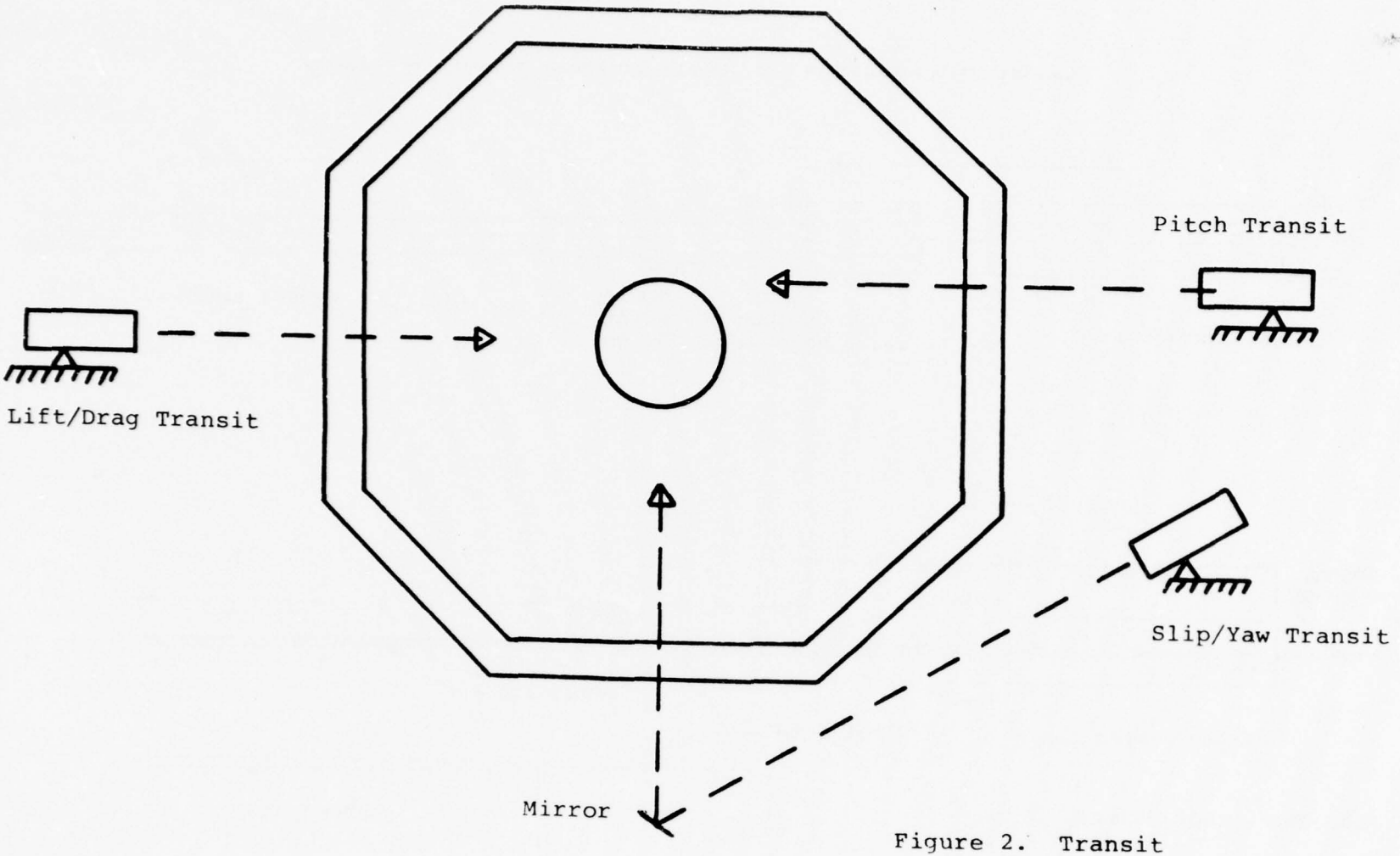

Figure 2. Transit Positioning System

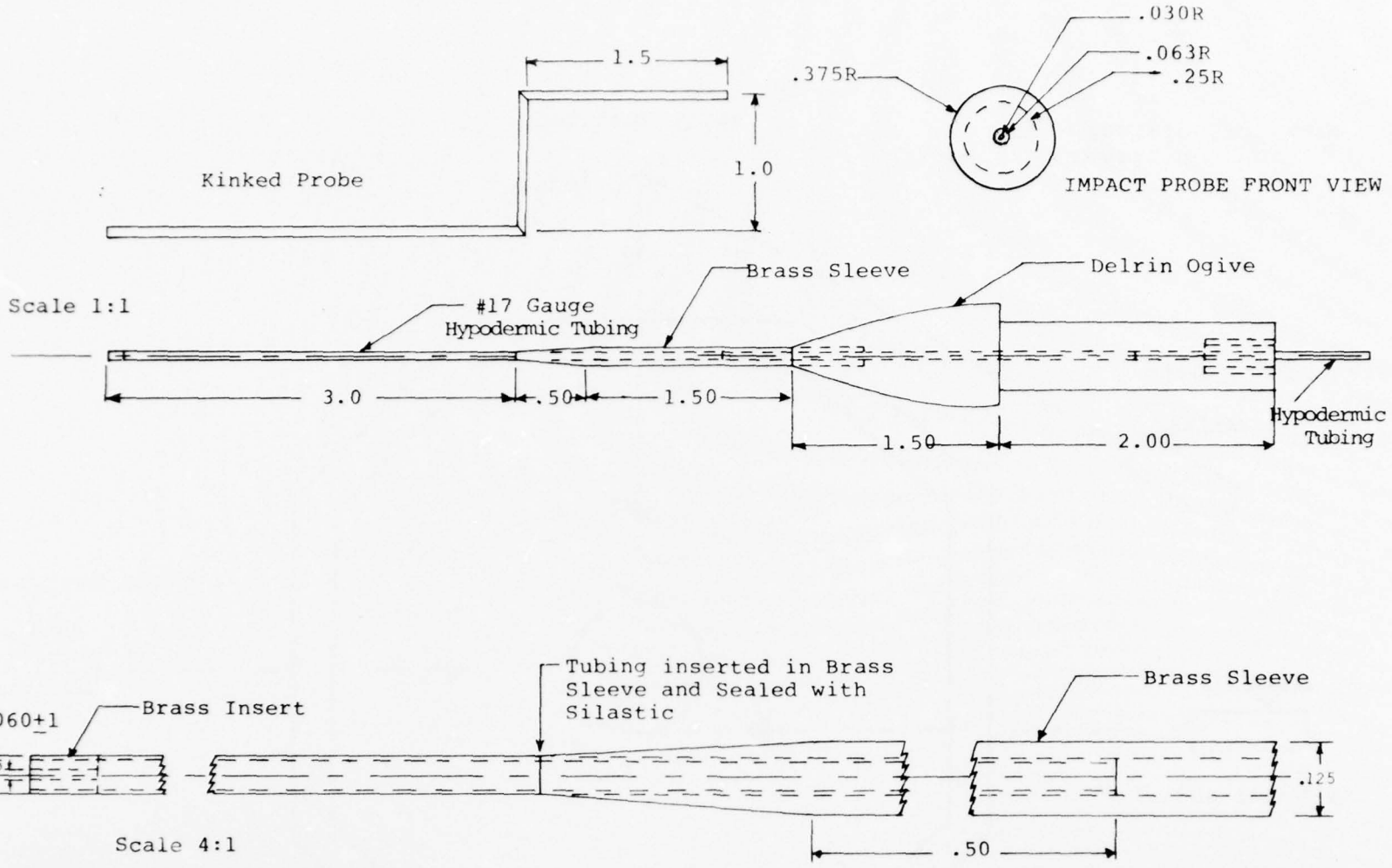

Figure 3. Impact Pressure Probe (All dimensions in inches)

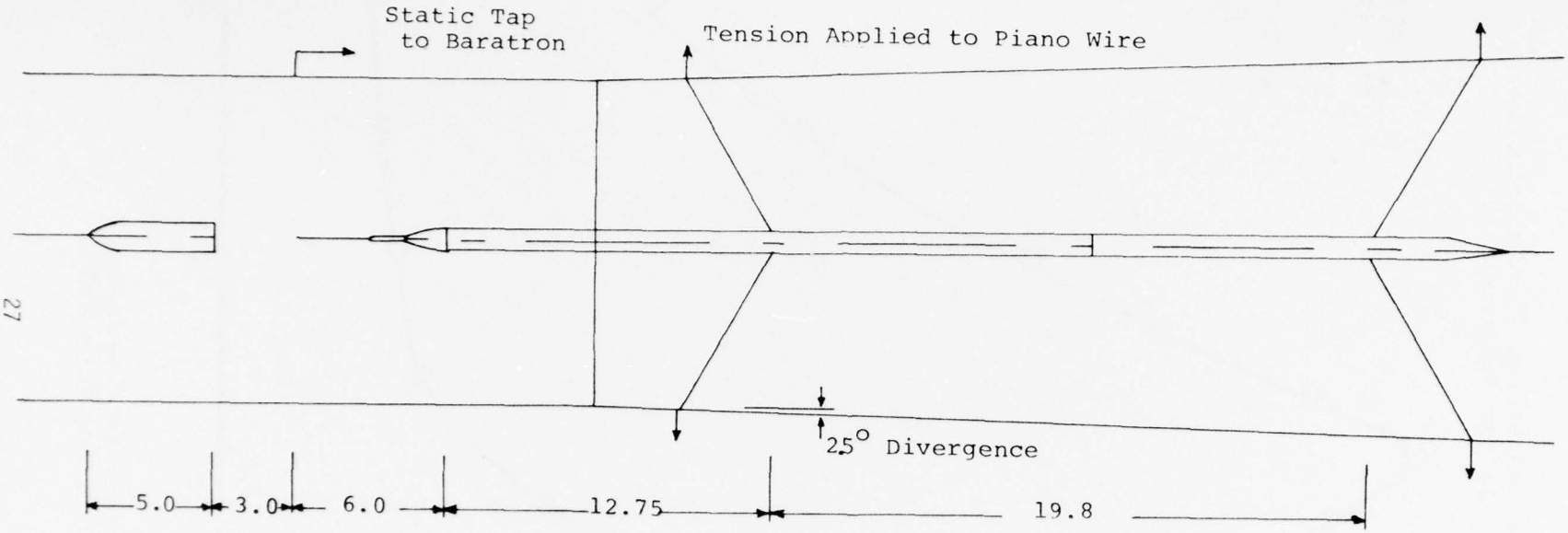

Figure 4. Probe Installation
All Dimensions in Inches

Figure 5. Wake Centerline Static Pressure
(after Reference 15)

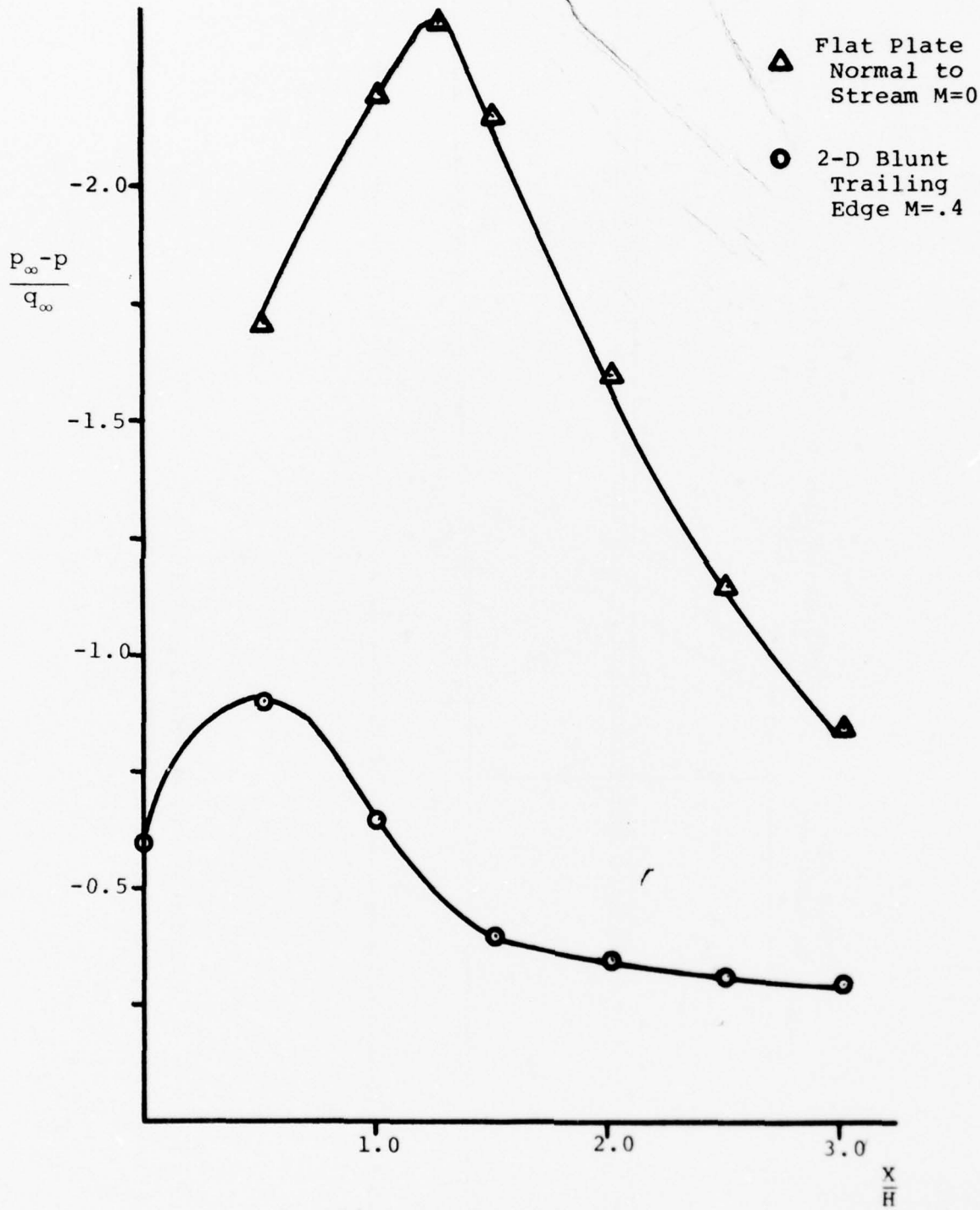

$\frac{X}{H} = \frac{\text{Distance Downstream}}{\text{Trailing Edge Width}}$

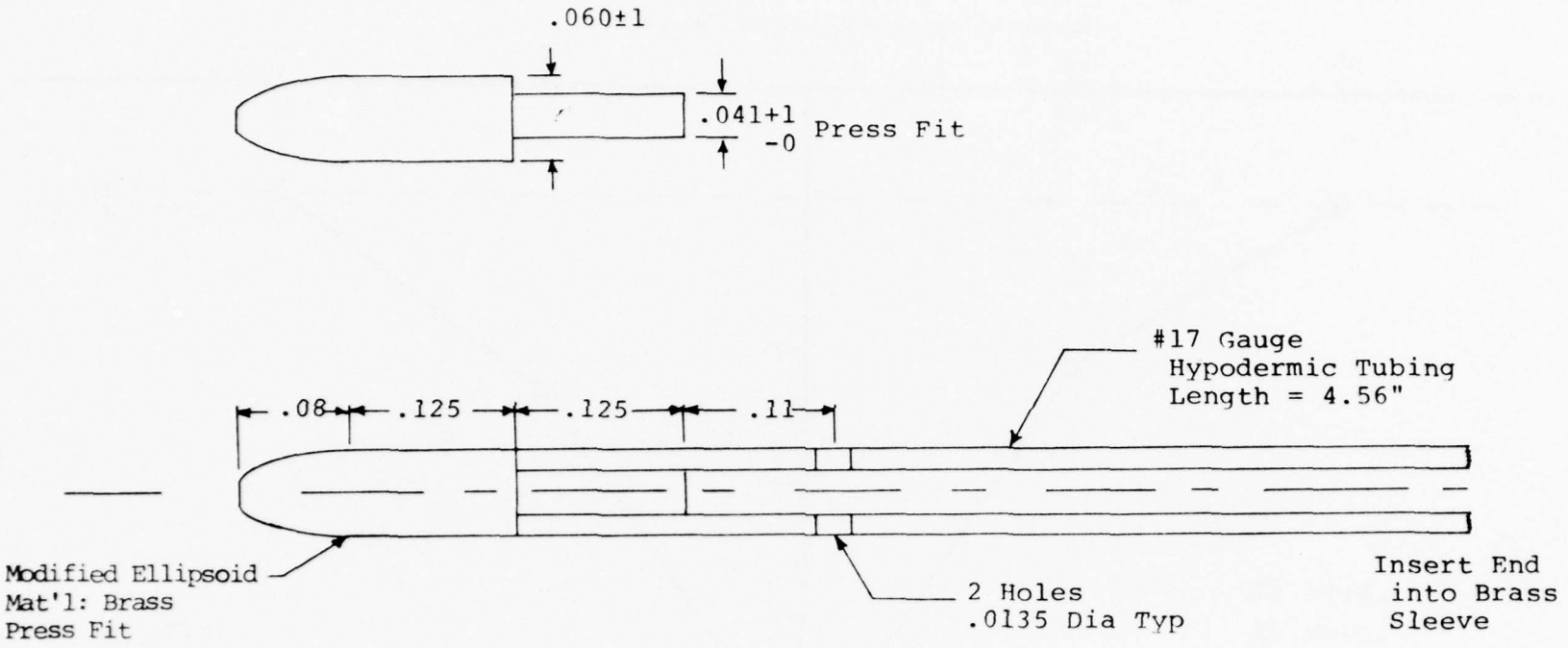

Figure 6. Static Pressure Probe
Scale 8:1, All Dimensions in Inches

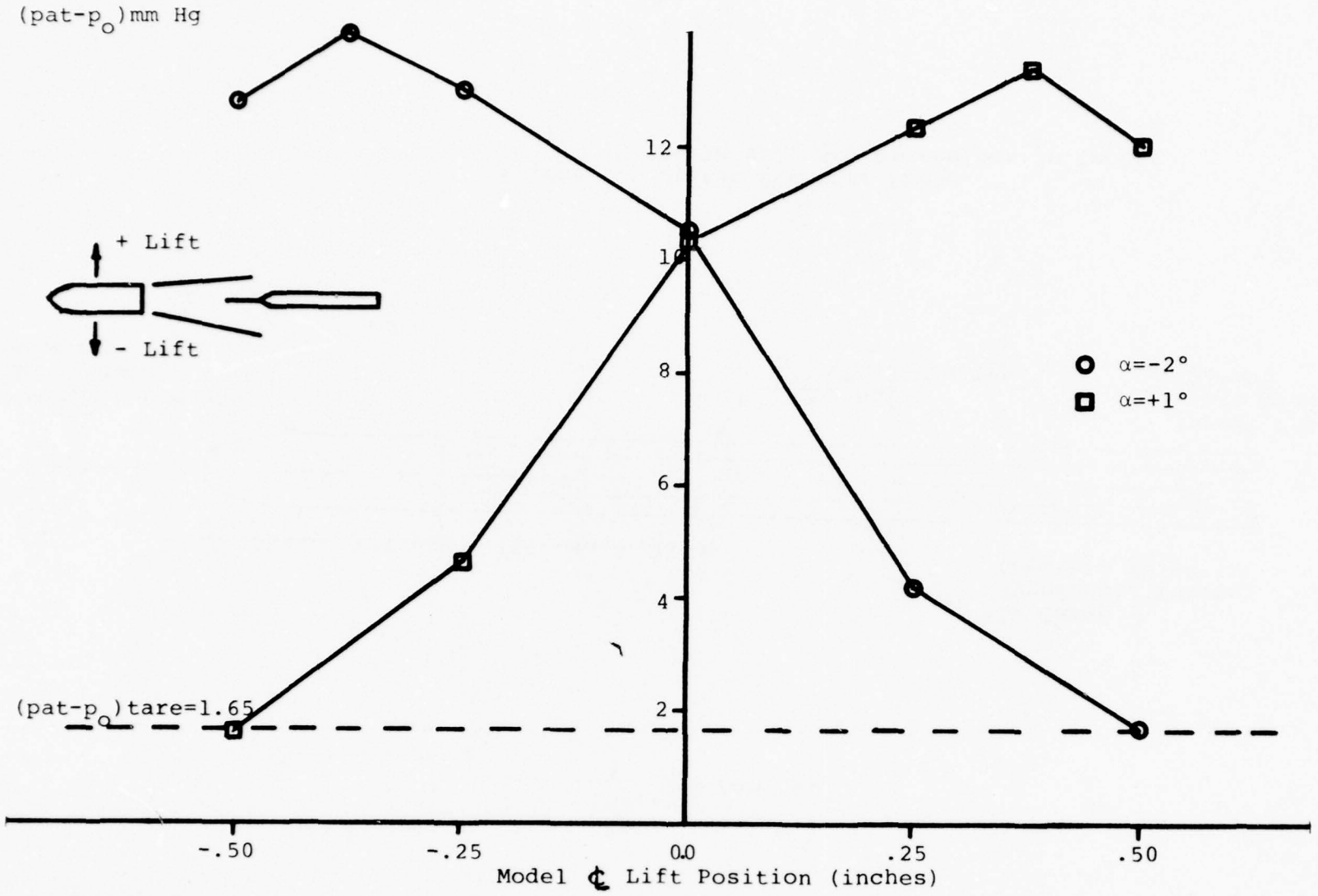

Model on Tunnel Vertical ℄
β=0°

Figure 7. Flow Misalignment in Lift

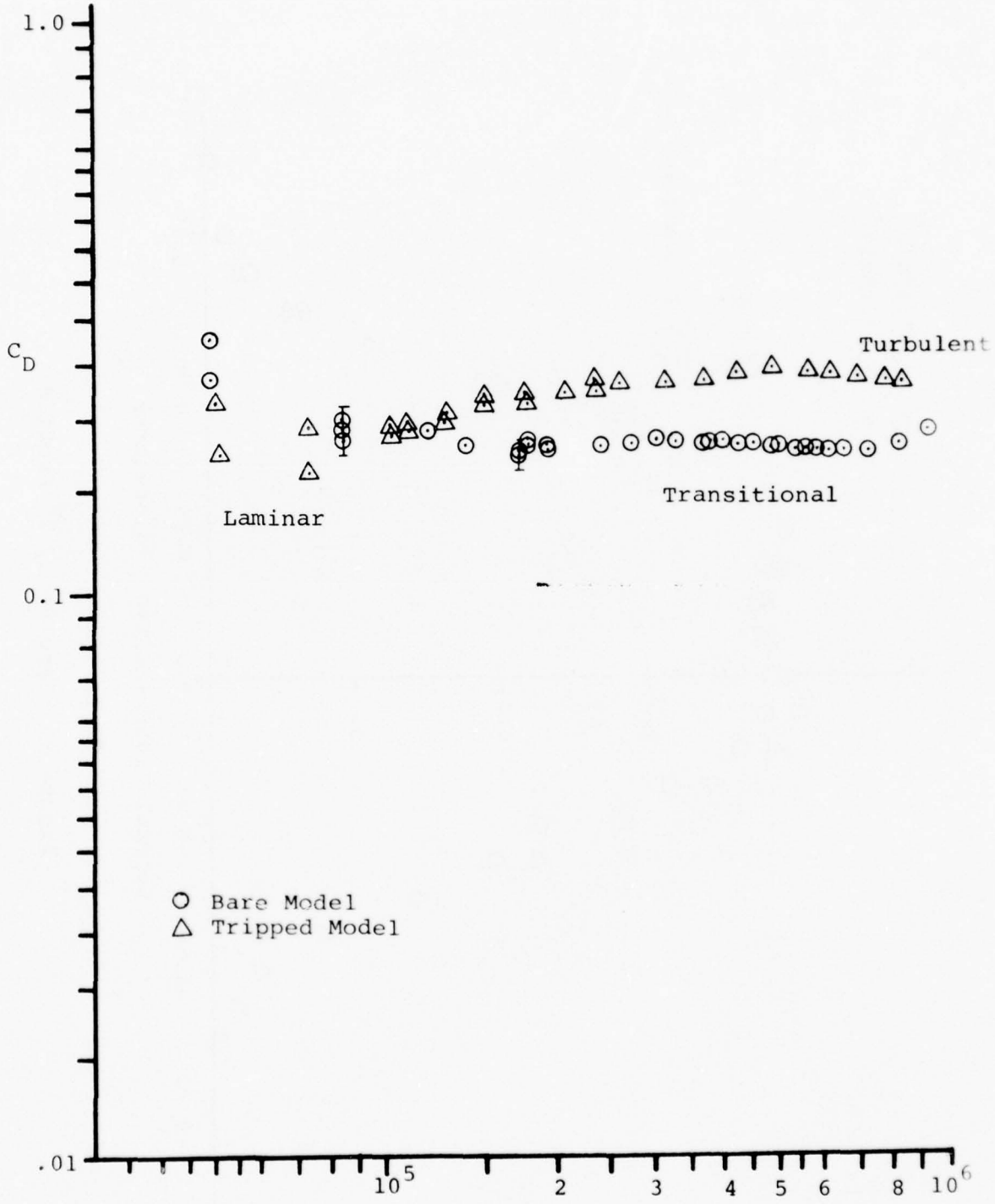

Figure 8. C_D vs. Re_L - 5 Caliber Ogive Cylinder

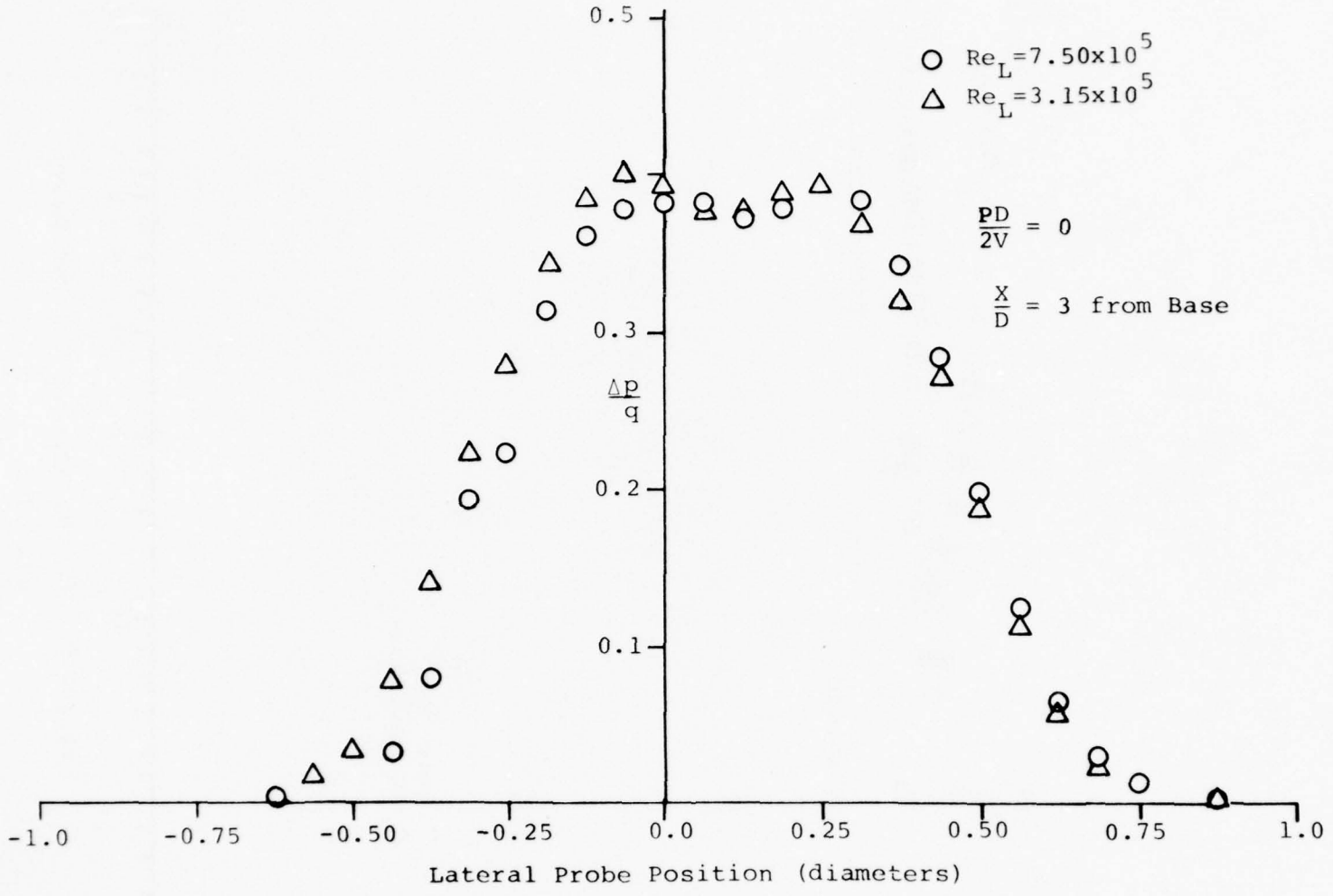

Figure 9. Zero Spin, 7^{o} Profile

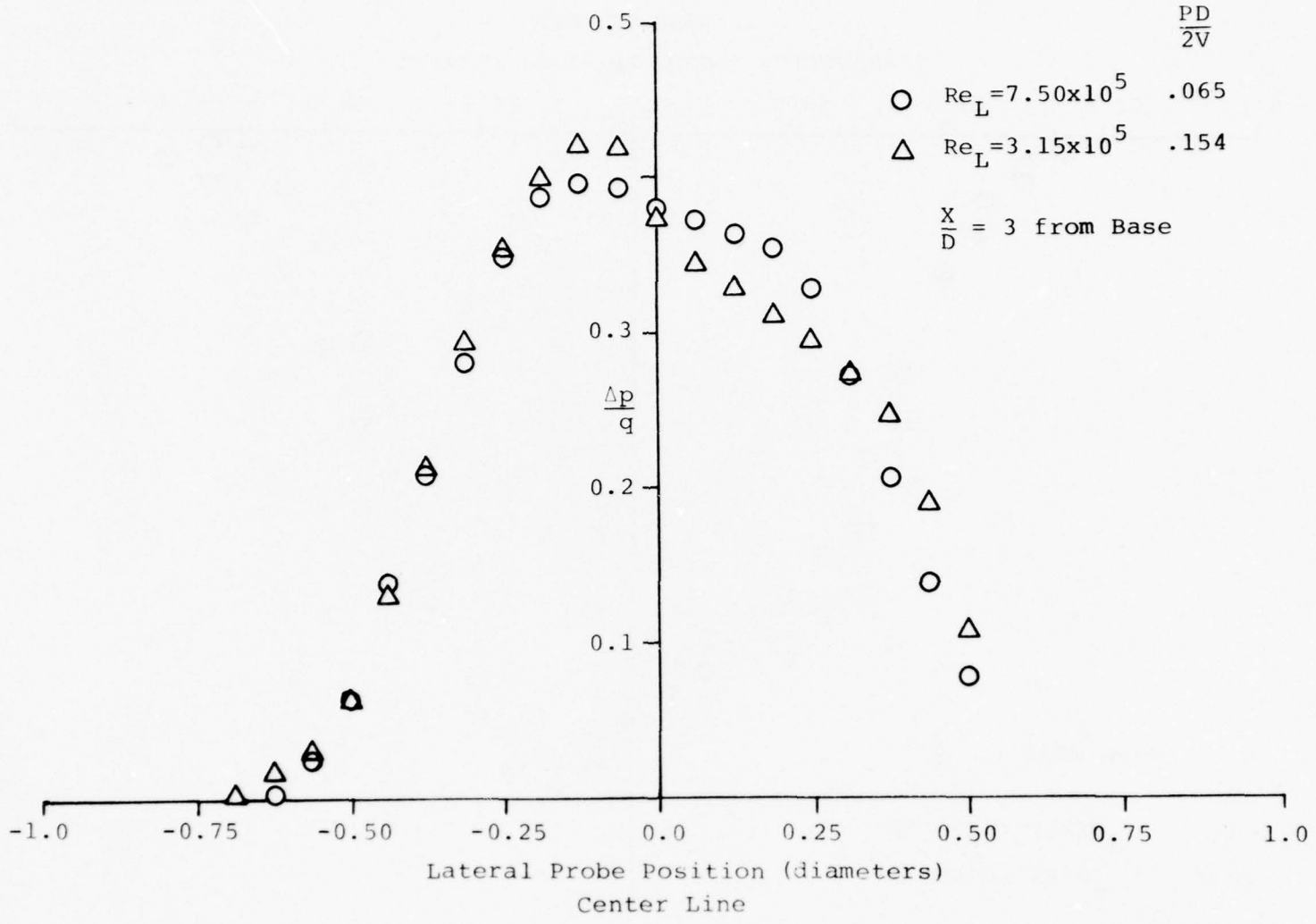

Figure 10. Low Spin, 7° Profile

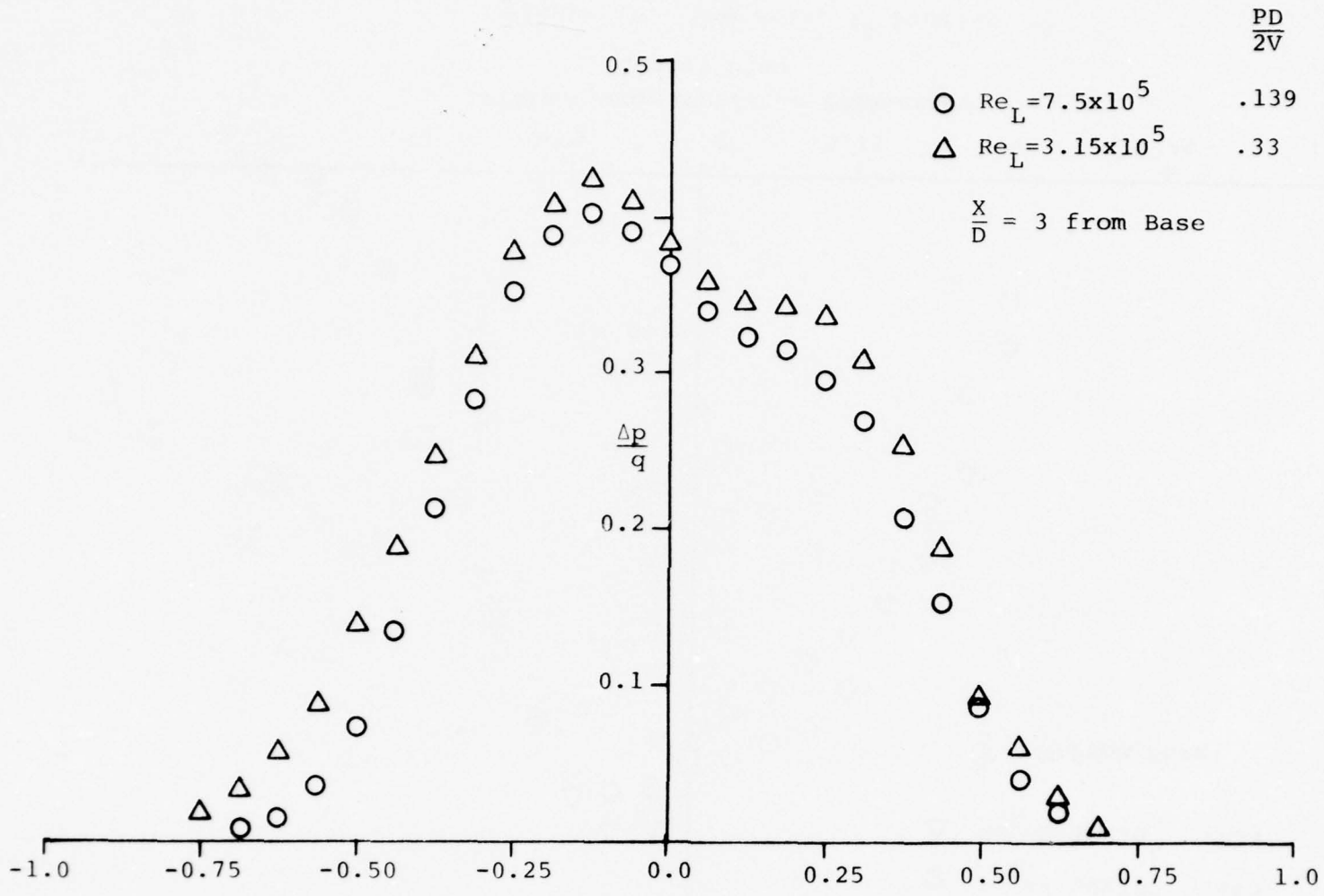

Figure 11. High Spin, 7° Profile

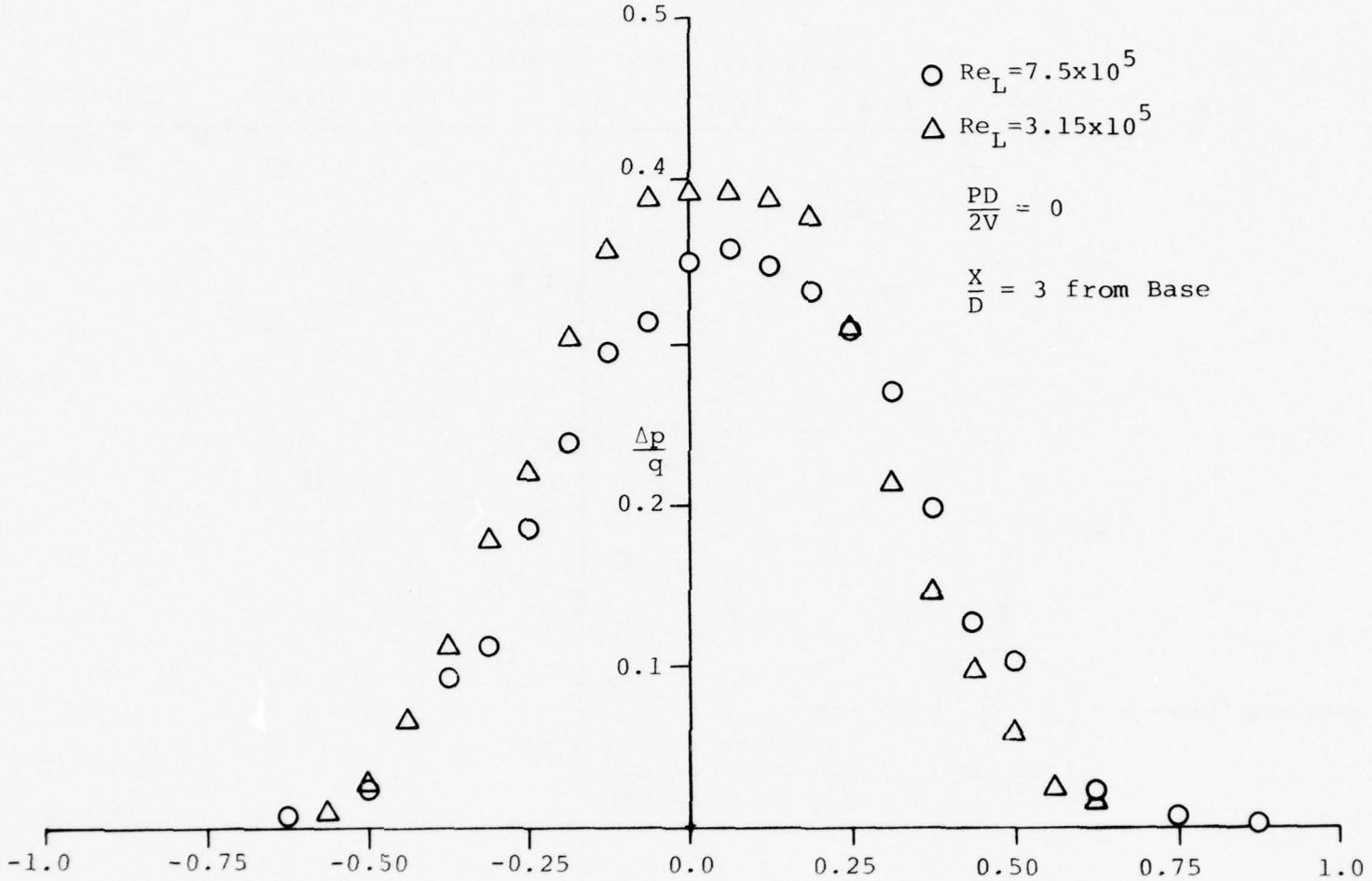

Figure 12. Zero Spin, 2^{o} Profile

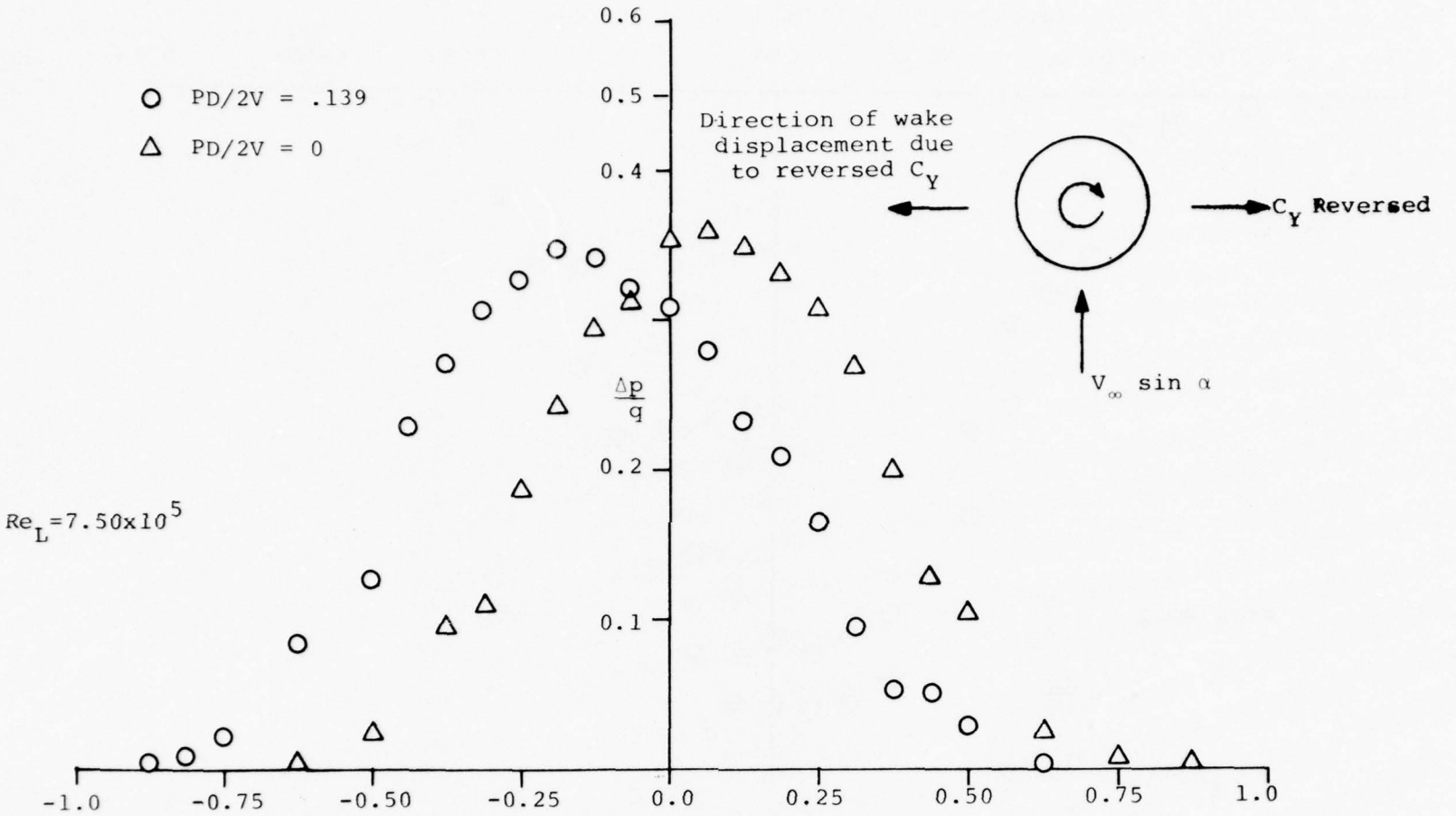

Figure 13. Magnus Reversal Effect at 2^o

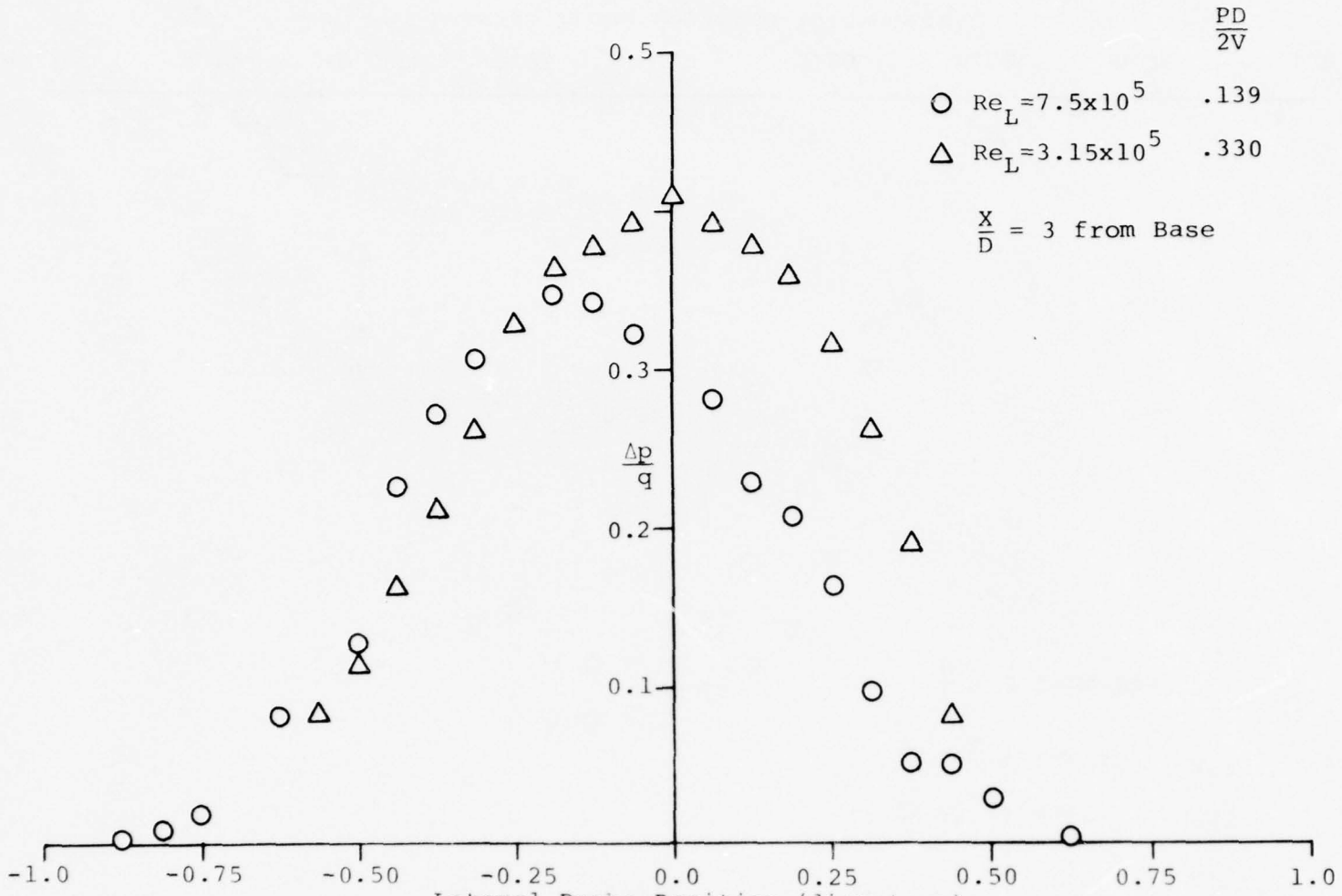

Figure 14. High Spin, 2^{o} Profile

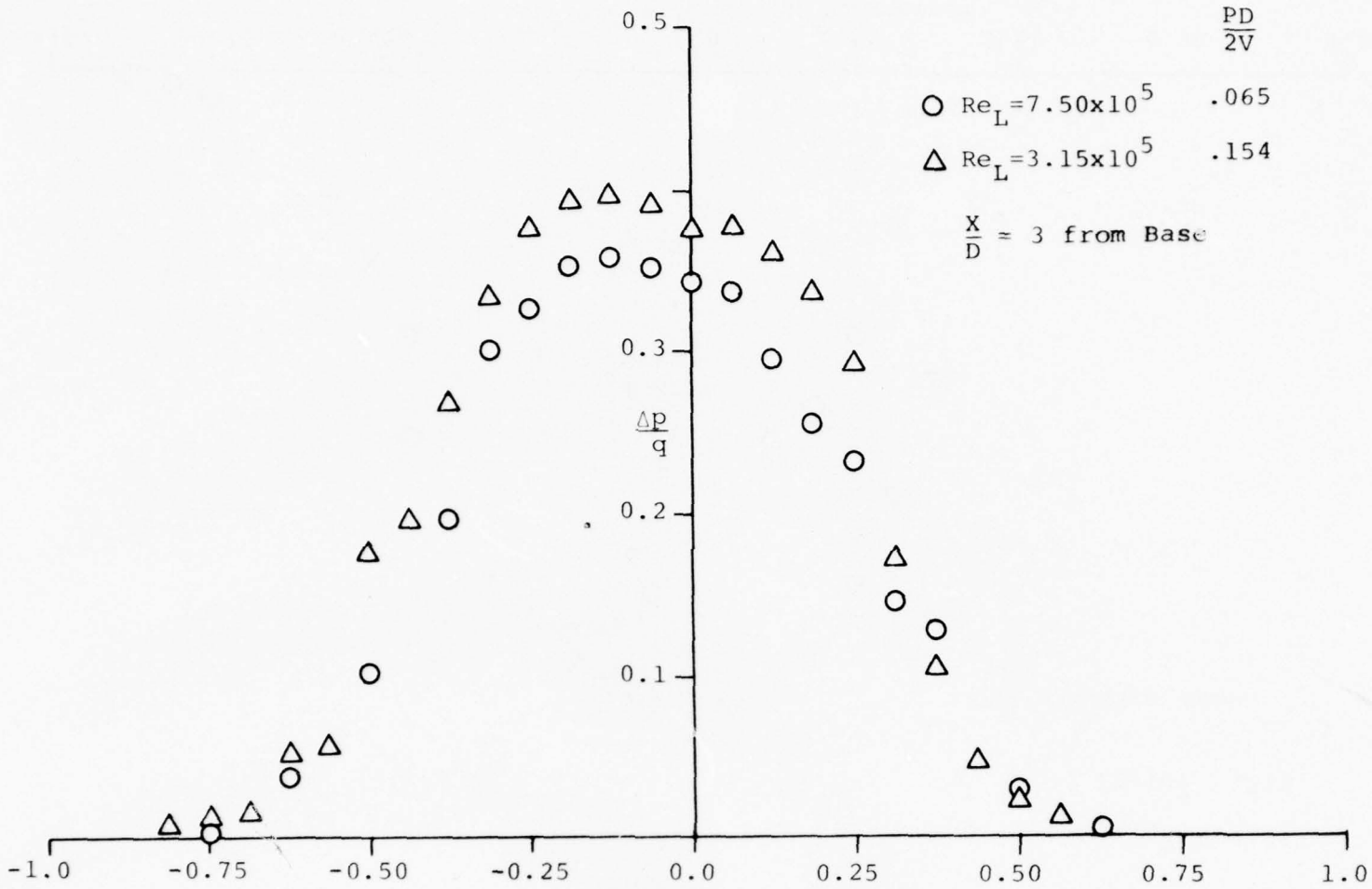

Figure 15. Low Spin, 2^{o} Profile

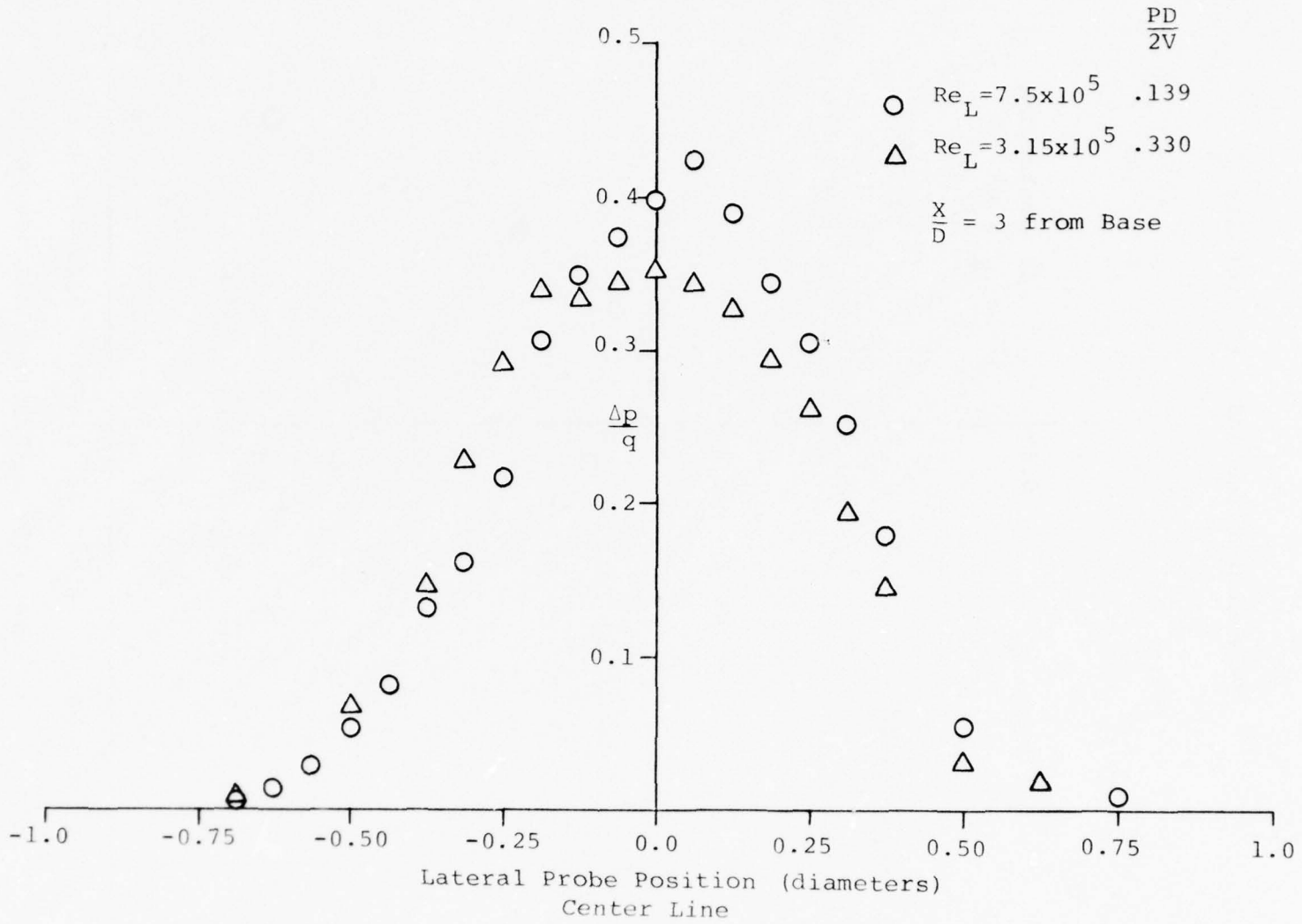

Figure 16. High Spin, 0° Profile

Wake Centerline and + ½" Profiles

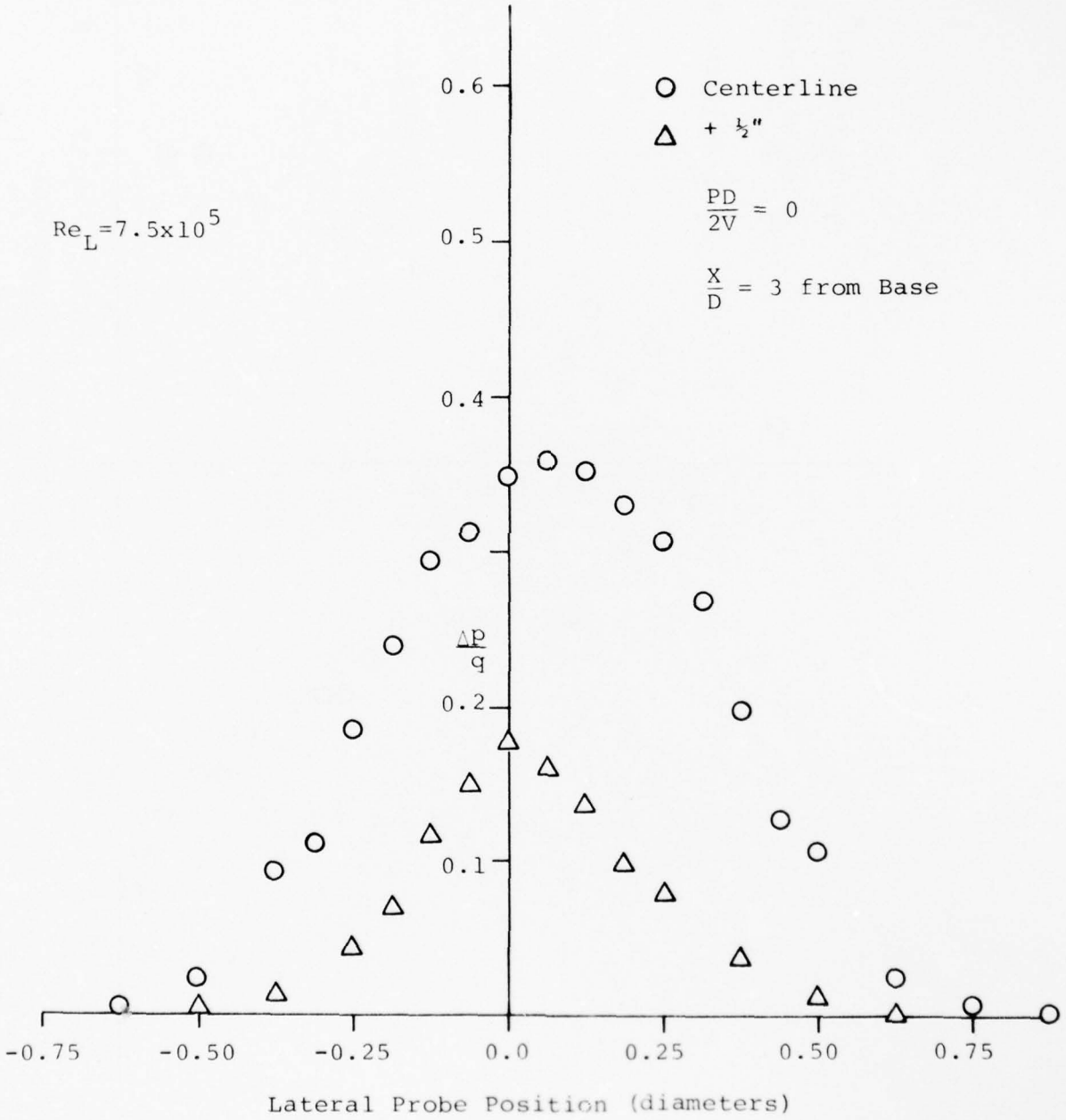

Figure 17. Zero Spin, 2° Offset Profiles

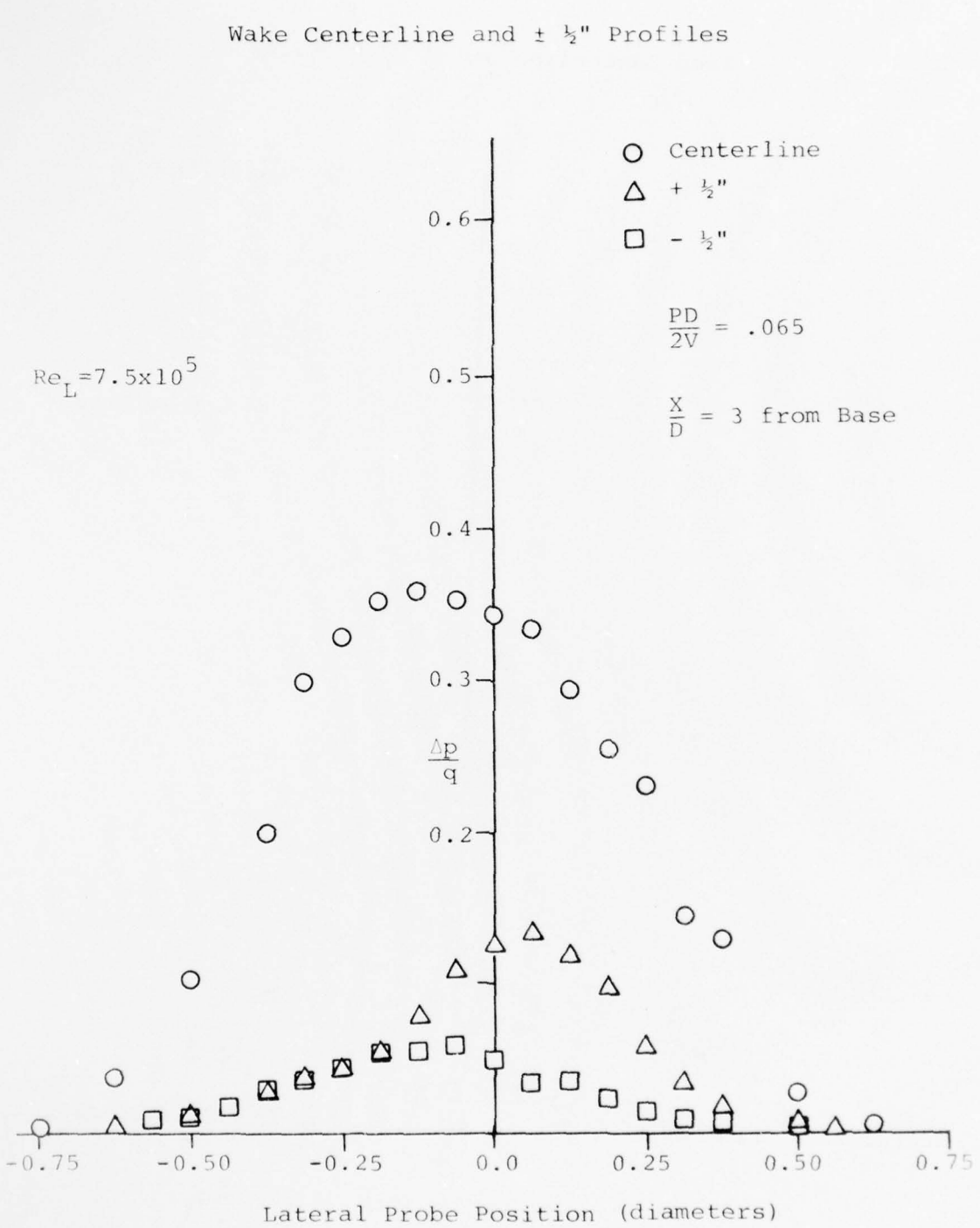

Figure 18. Low Spin, 2^{o} Offset Profiles

Wake Centerline and ± ½" Profiles

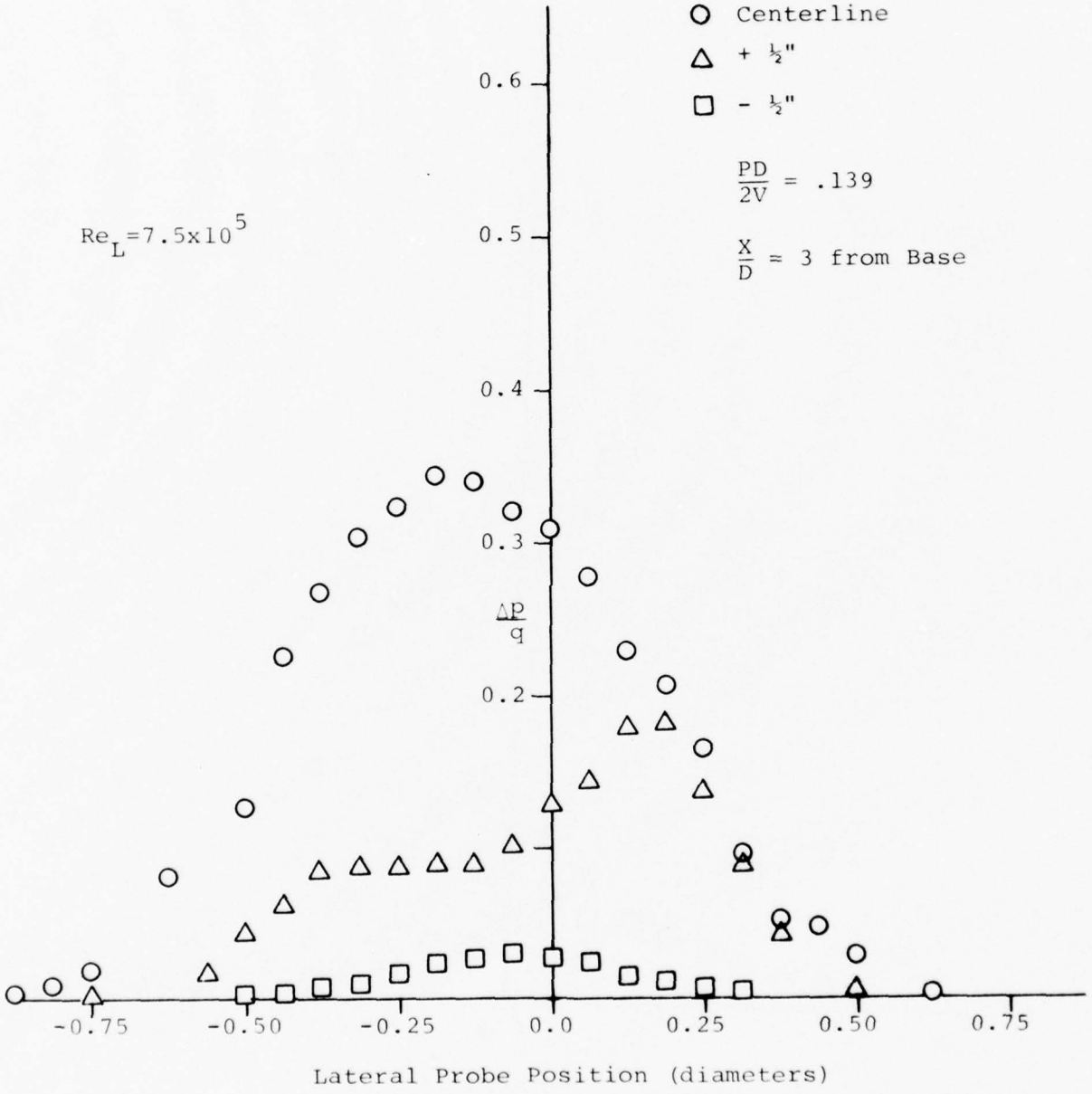

Figure 19. High Spin, 2^{o} Offset Profiles

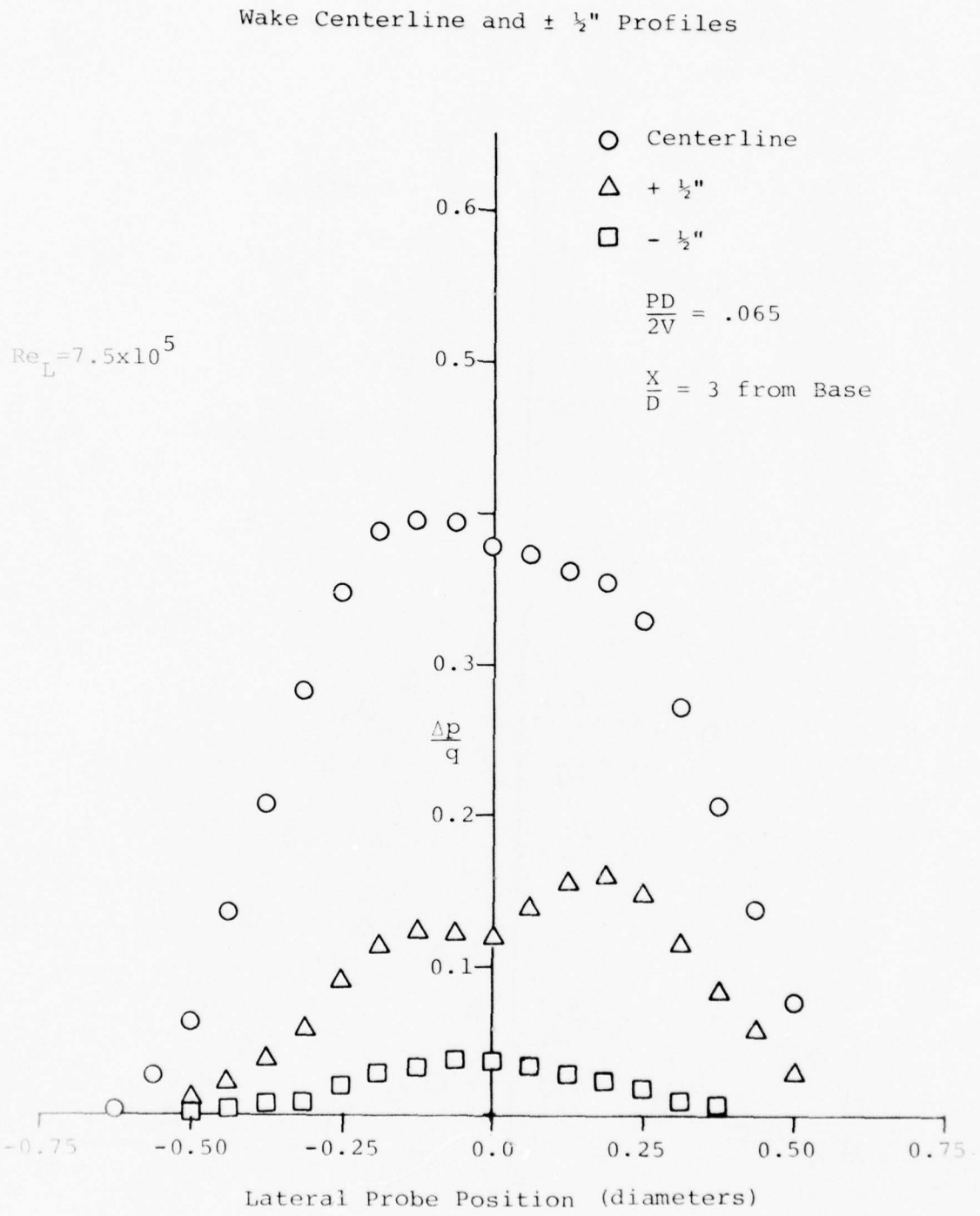

Figure 20. Low Spin, 7° Offset Profiles

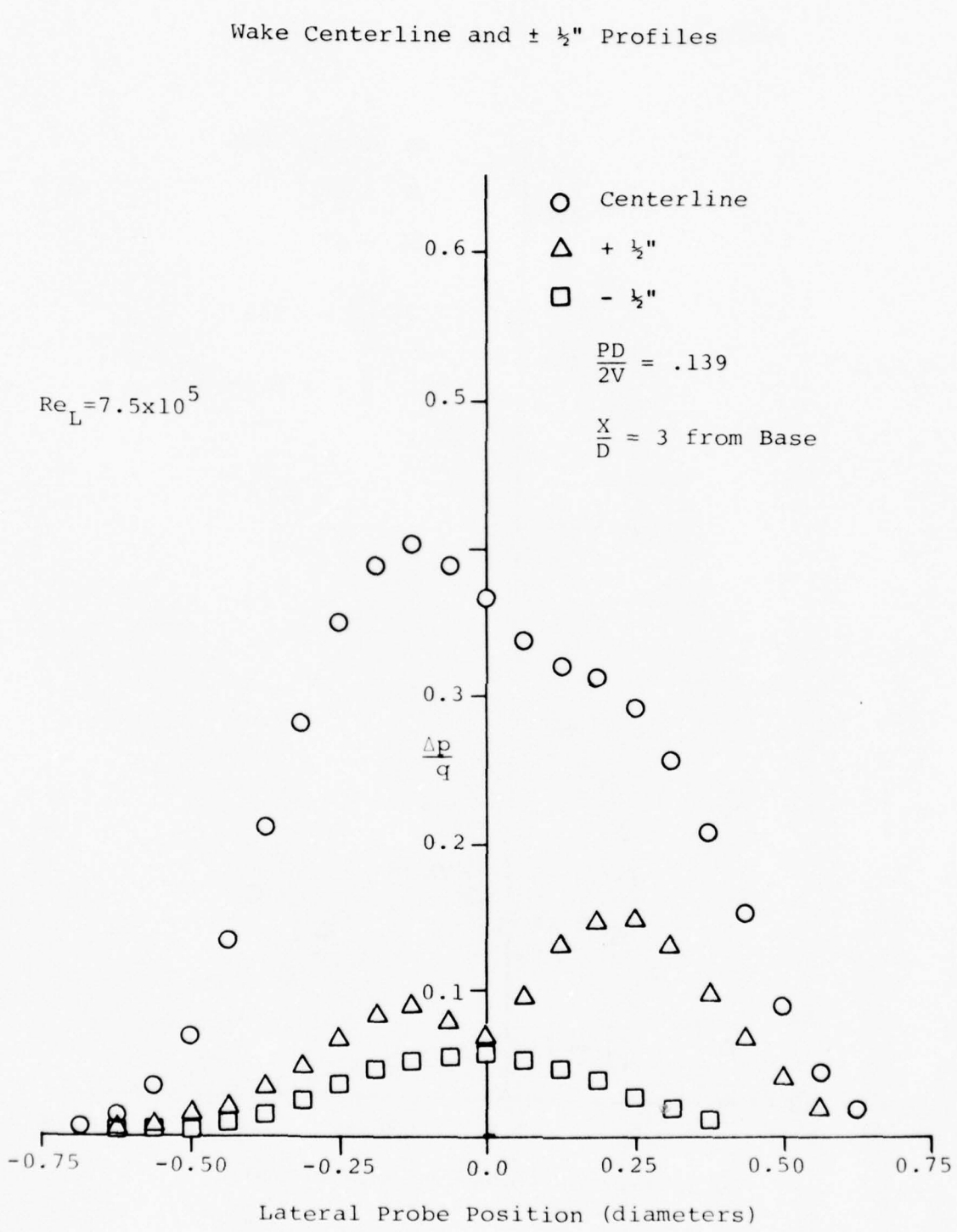

Figure 21. High Spin, 7° Offset Profiles

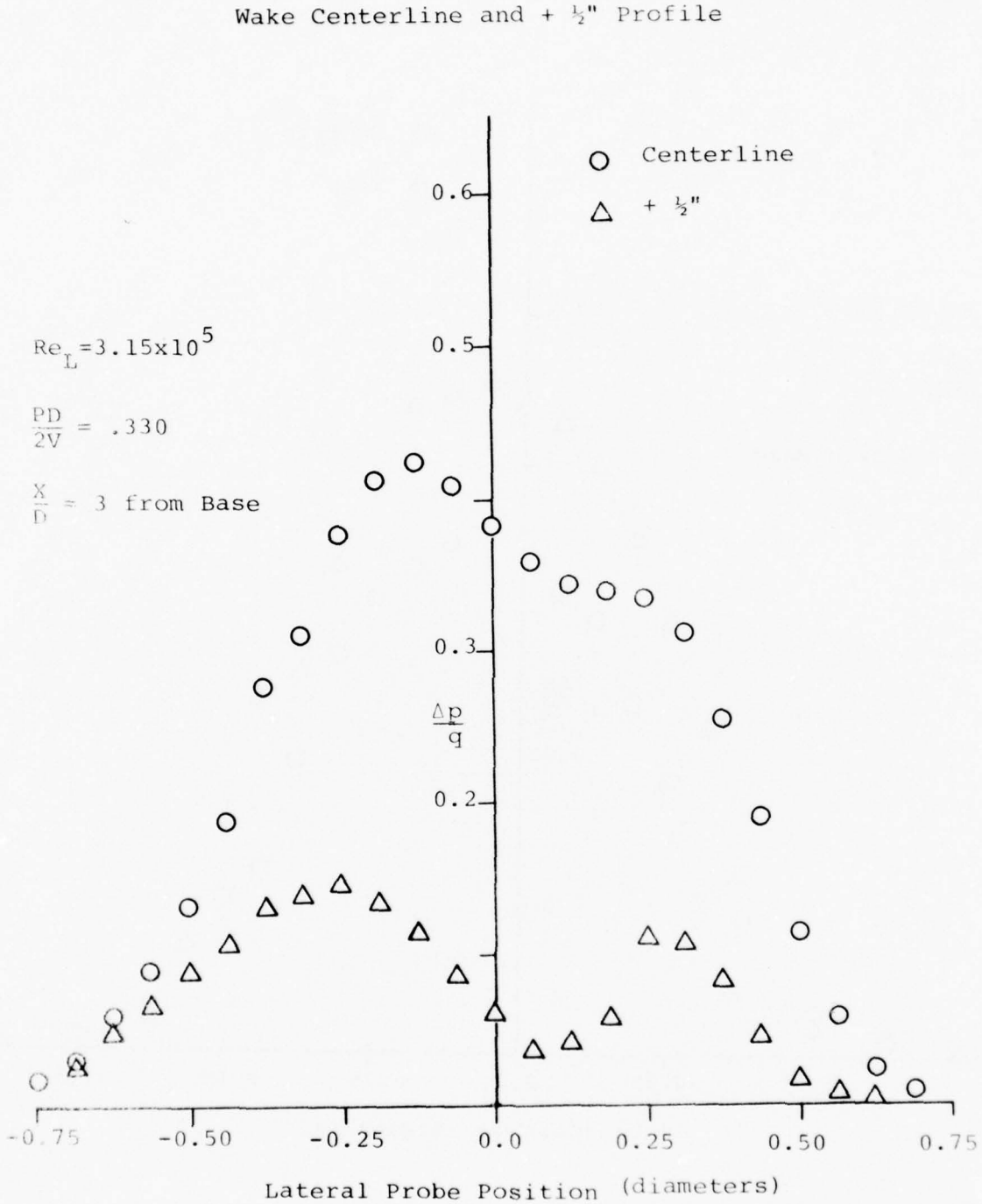

Figure 22. High Spin, 7° Offset Profiles

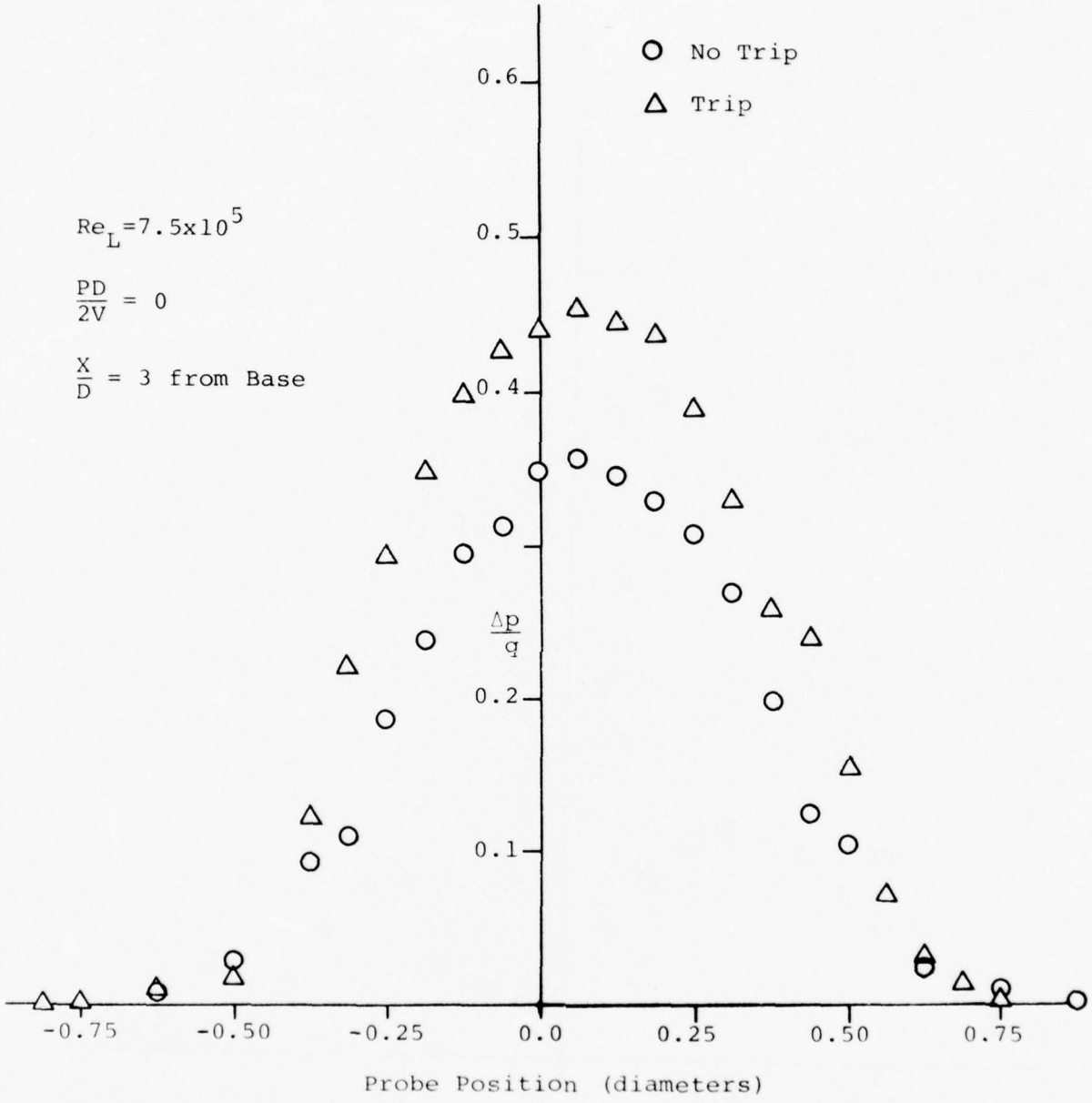

Figure 23. No Spin, 2^{o} Transition Effects

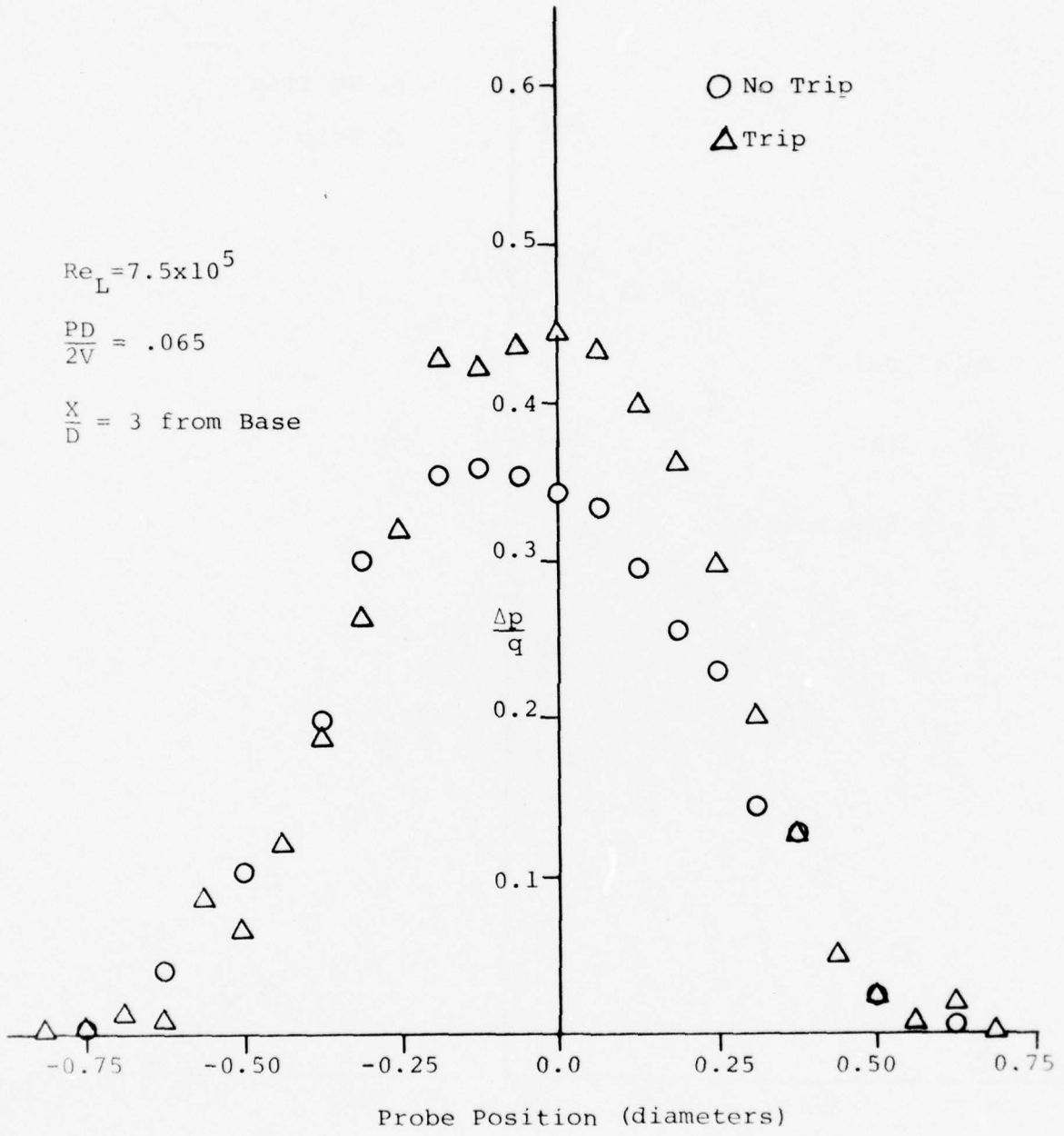

Figure 24. Low Spin, 2° Transition Effects

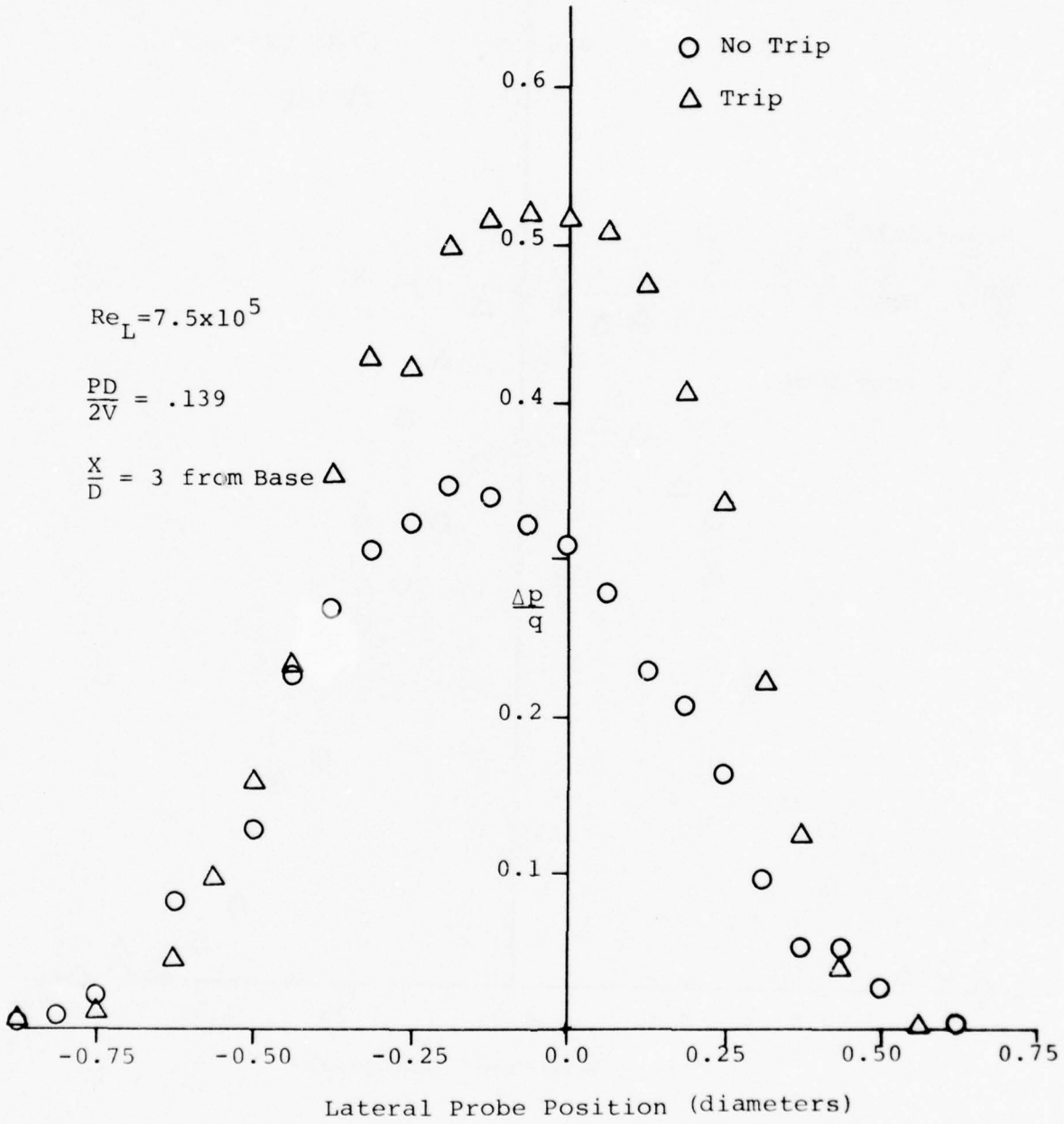

Figure 25. High Spin, 2^{o} Transition Effects

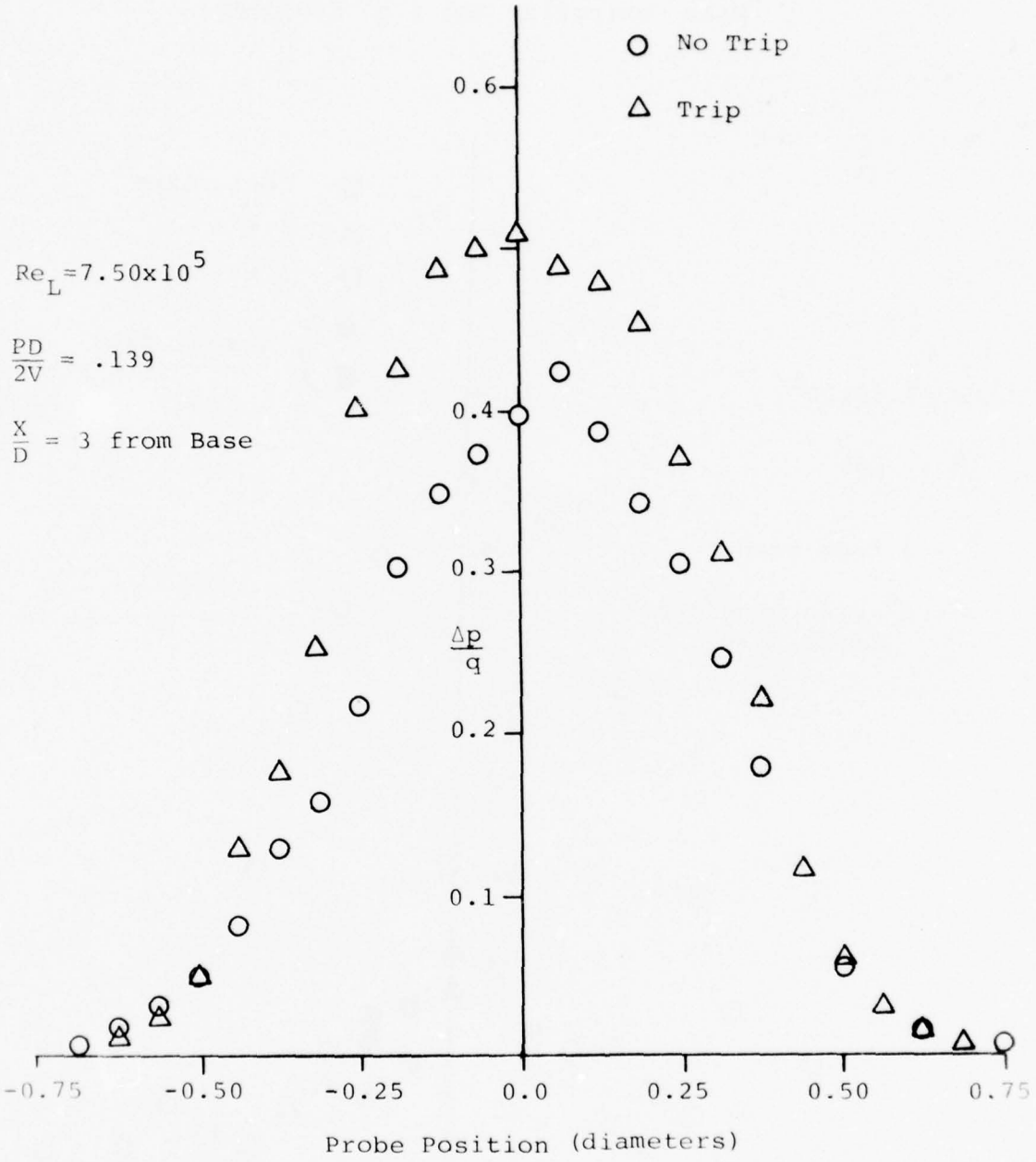

Figure 26. High Spin, 0° Transition Effects

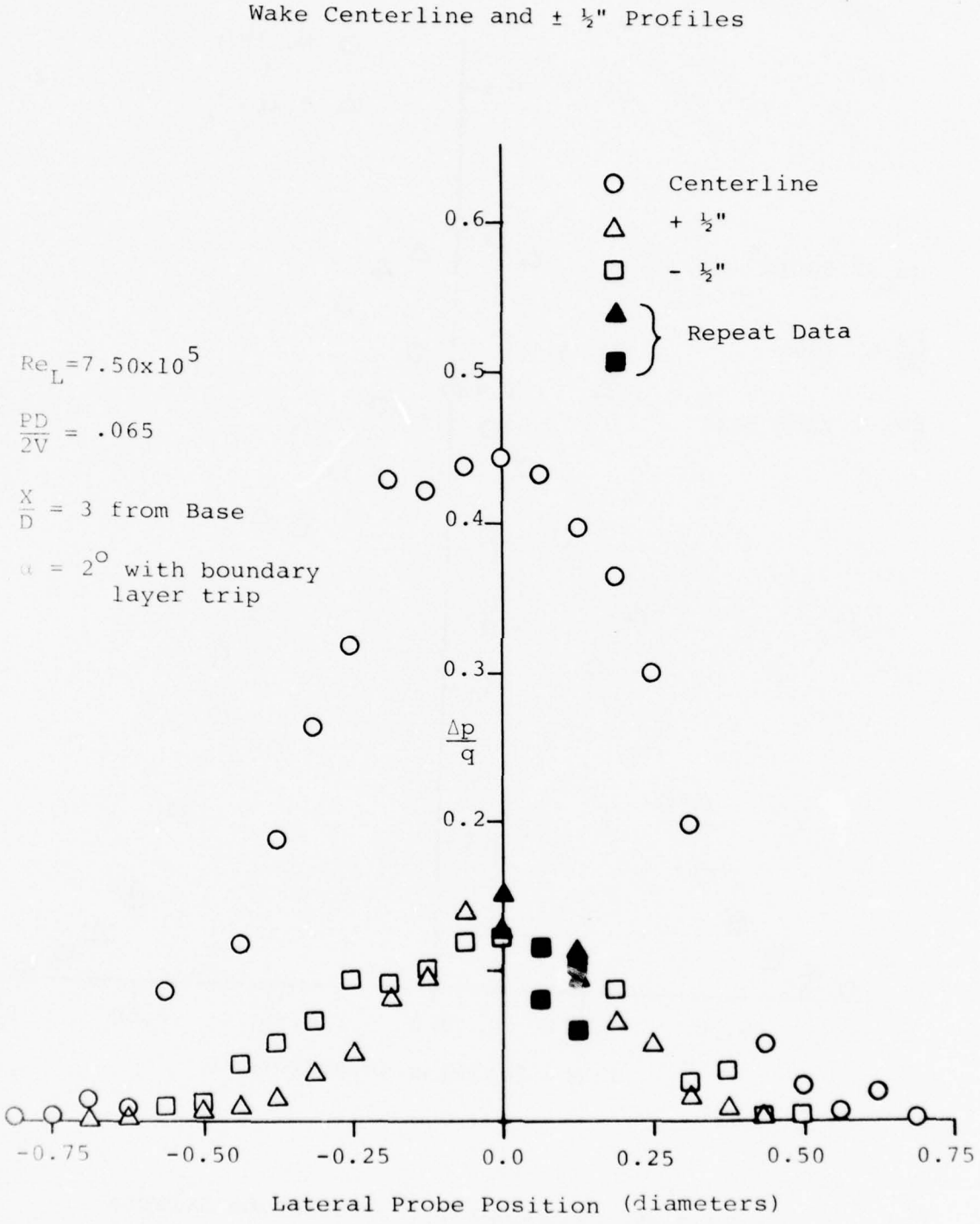

Figure 27. Transition Effect on Repeatability

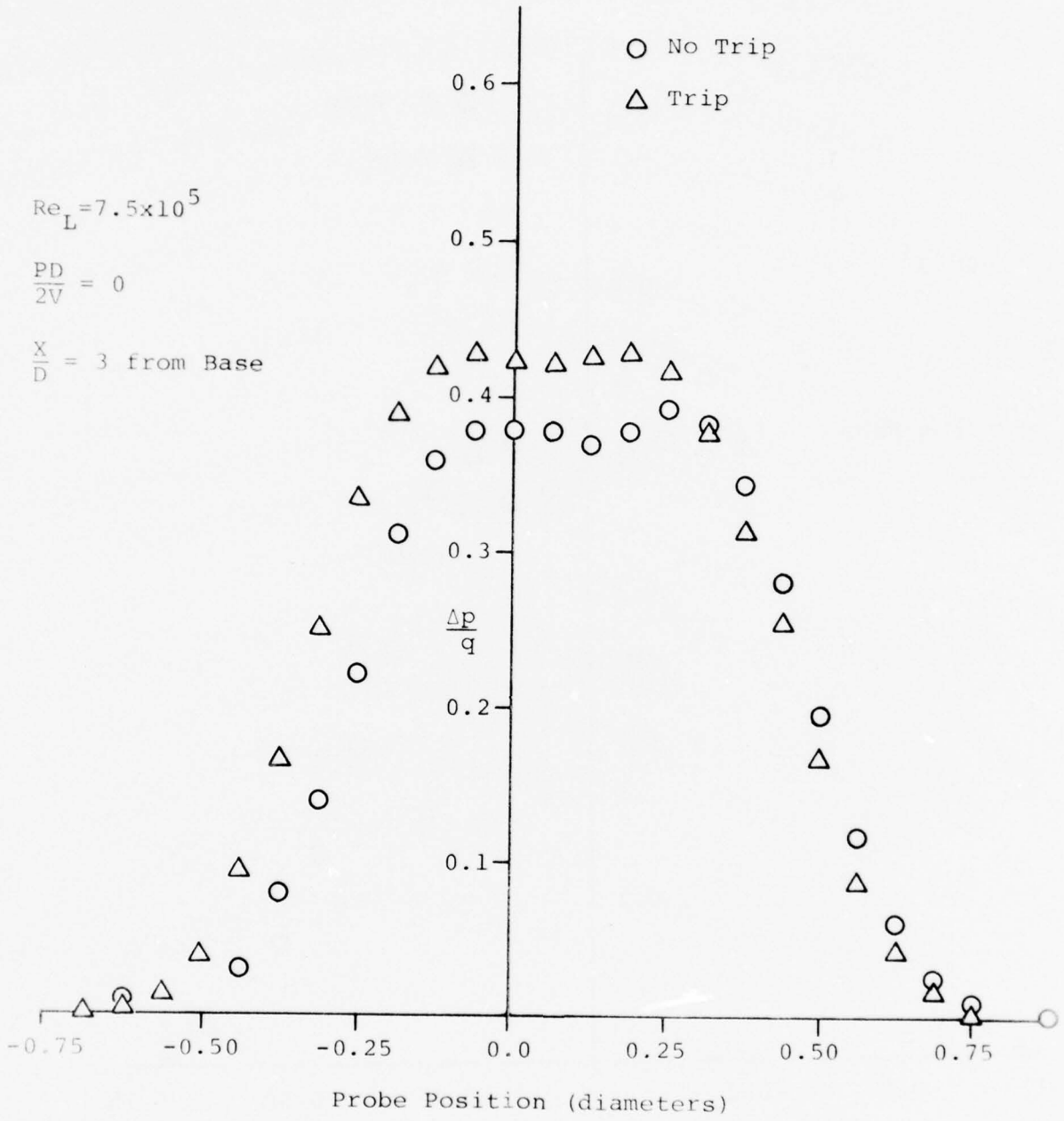

Figure 28. No Spin, 7^{o} Transition Effects

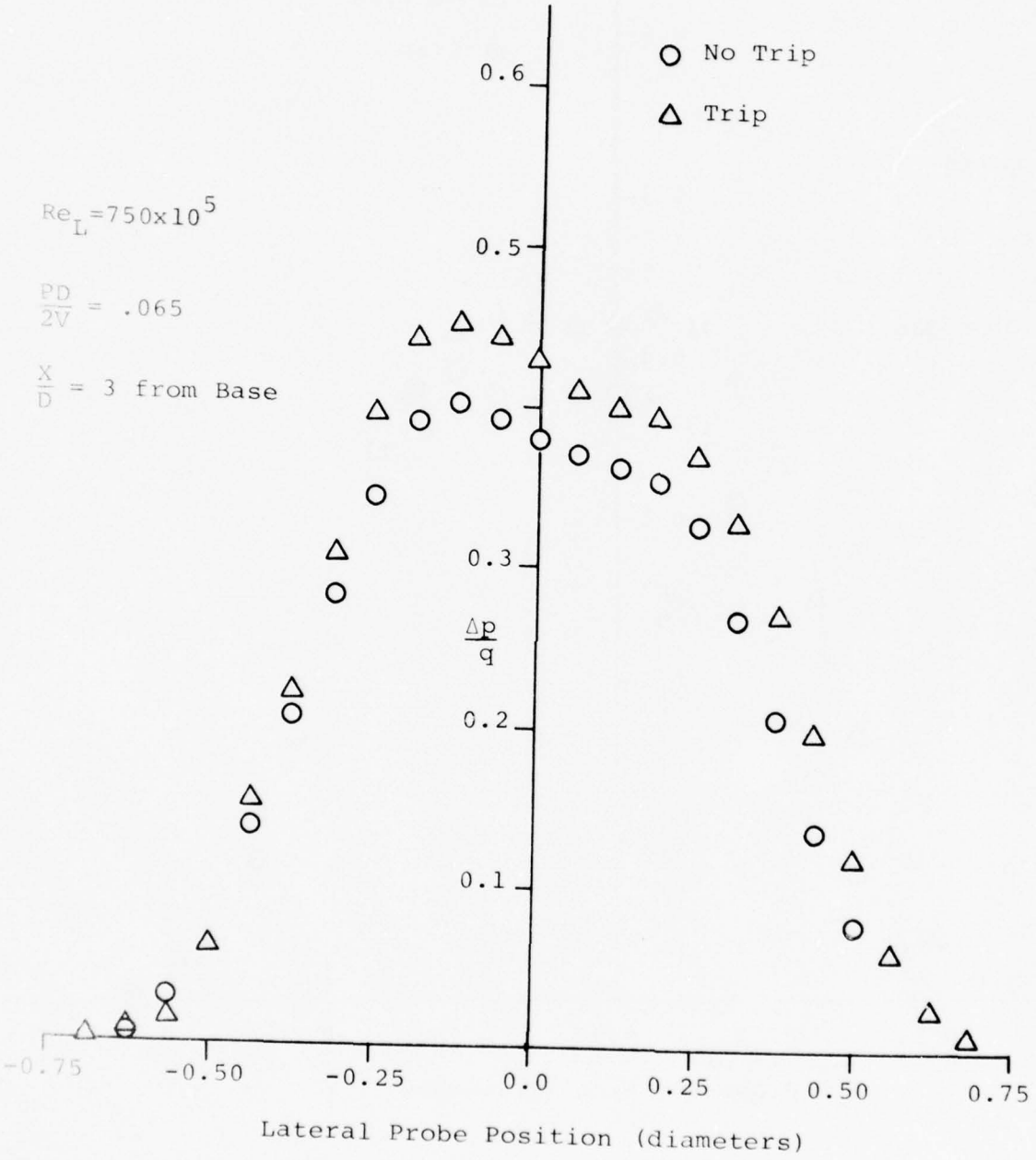

Figure 29. Low Spin, 7° Transition Effects

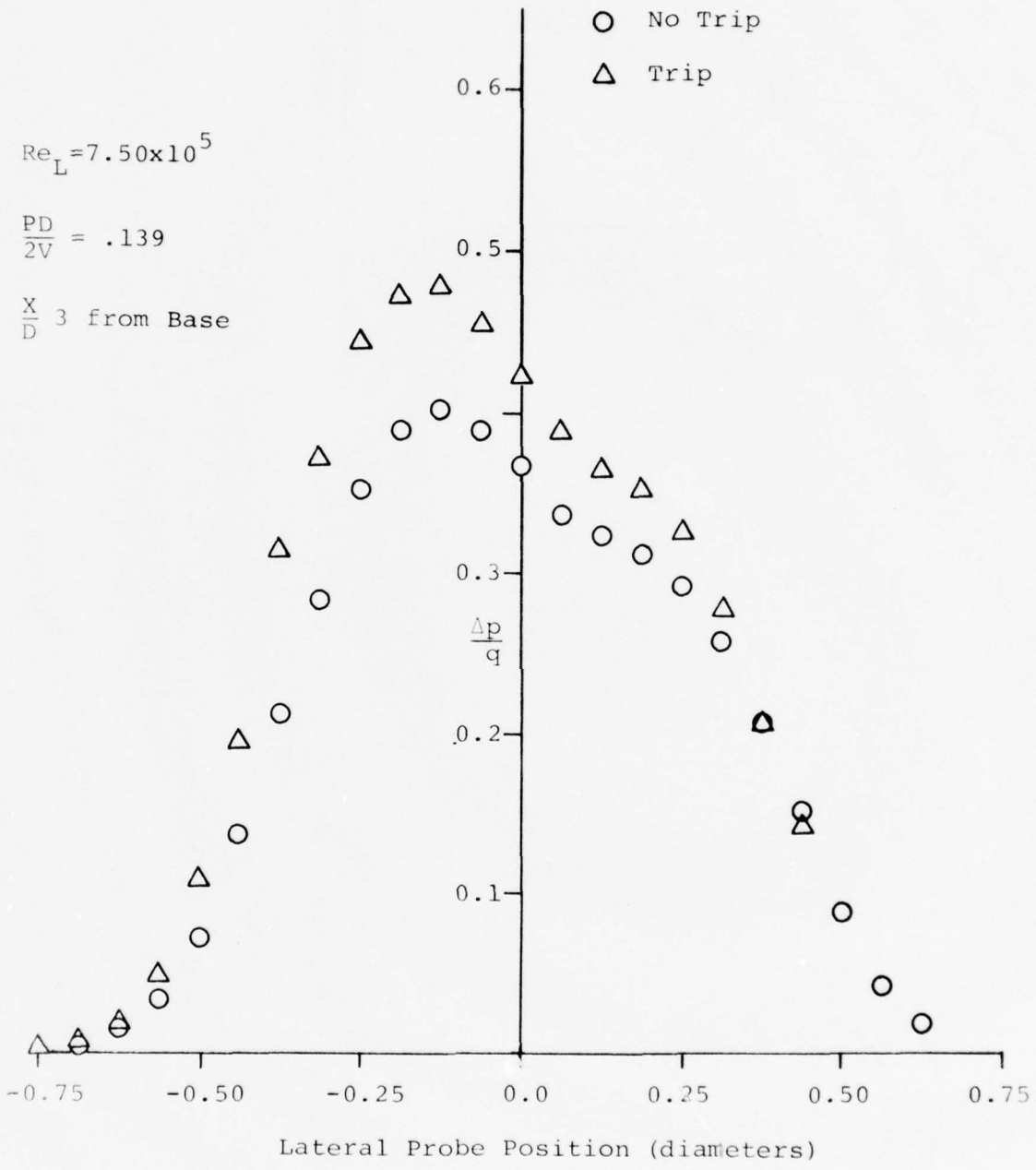

Figure 30. High Spin, 7° Transition Effects

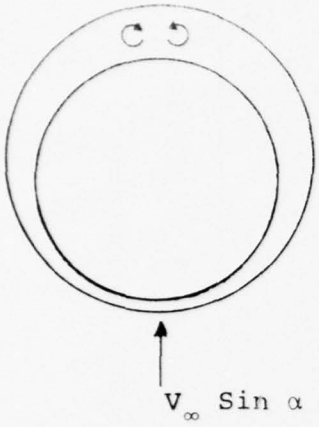

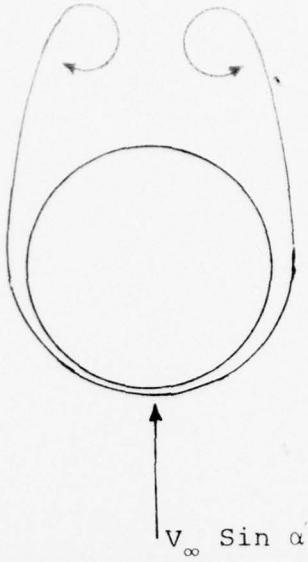

Low α: Attached Flow
Embedded Vorticity

High α: Separated Flow
Shed Vorticity

Figure 31. Zero Spin Rear View of Crossflow about Inclined Body of Revolution

Appendix A

PROFILE DRAG BY MOMENTUM DEFECT

Theoretical Development

The viscous flow of a fluid about a solid body results in a net loss of streamwise momentum equal in magnitude to the profile drag imposed on the body. Profile drag represents the sum of skin friction drag, owing to the integral of body surface shearing stresses, and form drag, due to normal forces in the downstream direction. The methods developed initially by Betz and Jones from consideration of the momentum equation provide a means of calculating the profile drag from the velocity profile of two-dimensional or axially symmetric wake geometries. A unique feature of this method of drag determination is the essential isolation of profile and lift induced components of drag. Two-dimensional tests (10), for example, exhibit errors of the order of 4% for a lift coefficient of 0.8.

A brief discussion of the origin and subsequent practical adaptation of the momentum defect theory is presented below. Consider the integral form of the momentum equation (22)

$$\int \frac{\partial (u_i \rho)}{\partial t} \, dV = - \int \rho u_i u_j n_j dA + \int F_i \, \rho dV + \int \sigma_{ij} n_j dA \qquad (A.1)$$

where $\vec{F}$ = volume force per unit mass of fluid

$$\sigma_{ij} = -\rho \delta_{ij} + 2\mu \left[\frac{1}{2} \left(\left(\frac{\partial u_i}{\partial x_j} + \frac{\partial u_j}{\partial x_i} \right) \right) - \frac{1}{3} \frac{\partial u_i}{\partial x_i} \delta_{ij} \right] \qquad (A.2)$$

The momentum balance is determined for steady, viscous, incompressible fluid flow through the control volume defined by surfaces S_1 and S_2 in Figure A-1. The cylindrical control surface S_1 is far removed from the body, such that viscous forces at the surface may be considered negligible. The net momentum flux through S_2, comprising the contour of the model, is zero. Clearly, the contribution of S_2 in the momentum balance is a drag force on the fluid equal and opposite to that experienced by the body. Thus, for the flow assumptions above, Equation A.1 applied in the x direction becomes

$$D_o = \int(p_1+\rho u_1^2-p_2-\rho u_2^2)dA - \rho\int u\,\vec{u}\cdot\hat{n}dS + F_V \qquad (A.3)$$

where F_V = viscous forces acting at the control surface ≈ 0. The subscripts 1 and 2 denote streamwise flow properties at the upstream and downstream faces of S_1 respectively. Zero net mass flux through S_1 is expressed as

$$\int\vec{u}\cdot\hat{n}\,dS + \int(u_2-u_1)\,dA = 0 \qquad (A.4)$$

Letting the cylindrical control volume become infinitely long,

$$u_1 = V_\infty$$

$$p_1 = p_2 \qquad (A.5)$$

In the limit, as the cylindrical faces of S_1 recede from the model to infinity, substitution of the zero flux condition (Equation A.4) in the drag expression above results in the classical relationship between body profile drag and wake velocity.

$$D_o = \rho b\int u_2\,(V_\infty-u_2)dy \quad \text{two-dimensional wake}$$

$$D_o = 2\pi\rho\int u_2\,(V_\infty-u_2)rdr \quad \text{axially-symmetric wake} \qquad (A.6)$$

For practical purposes methods utilizing independent initial assumptions to evaluate the above integrals were developed by Betz and Jones (23). Both enable drag prediction from pitot static wake measurements close to the body (within a body length) where static pressure is substantially different from the free stream value.

In order to evaluate the drag solely over the velocity profile depression (Figure A-2a), Betz introduced a hypothetical flow $u_2'(y)$ at Station 2, which corresponds with the actual velocity distribution everywhere but in the region of velocity defect,

where the total pressure has been increased to its free stream value. A source located at the body is effectively introduced in the flow as a result of u_2'. The thrust suffered by V_∞ due to the source is incorporated into a momentum balance for this hypothetical flow. By considering the difference between Equation A.3 above with $\vec{u} \cdot \hat{n} = 0$, and the momentum balance for the inviscid source flow, the drag expression (Equation A.6) is transformed into

$$C_{D_0} = 2\pi \left| \int_0^R \left(\frac{p_{o_\infty} - p_{o_2}}{q_\infty}\right) r\,dr + \int_0^R \left(\sqrt{\frac{p_{o_\infty} - p_2}{q_\infty}} - \sqrt{\frac{p_{o_2} - p_2}{q_\infty}}\right)\left(\sqrt{\frac{p_{o_\infty} - p_2}{q_\infty}} + \sqrt{\frac{p_{o_2} - p_2}{q_\infty}} - 2\right) r\,dr \right| \qquad (A.7)$$

which obviates evaluation of the integrals beyond the area encompassed by the depression in velocity.

Jones' method first applies conditions at Station 3 (Figure A-2b) far removed from the body ($p_3 = p_\infty$) to Equation A.6.

$$D_o = \rho \int u_3 (V_\infty - u_3)\, dA_3 \qquad (A.8)$$

Applying continuity along a stream tube between Stations 2 and 3,

$$\rho u_2 dA_2 = \rho u_3 dA_3$$

Thus,

$$D_o = \rho \int u_2 (V_\infty - u_3)\, dA \qquad (A.9)$$

The essential assumption of the method is that total pressure is invariant between Stations 2 and 3. Referring then to Figure A-2b, the resultant drag expression, again non-zero only for the velocity profile depression, is

$$C_{D_0} = 4\pi \int_0^R \sqrt{\frac{p_{o_2}-p_2}{q_\infty}} \left(1 - \sqrt{\frac{p_{o_2}-p_\infty}{q_\infty}}\right) r\,dr \qquad (A.10)$$

In considering the repercussions of the lossless flow assumption, Taylor (16) estimated that a maximum error of approximately 1.5% would be incurred in the drag calculation for two-dimensional wake measurements performed 1/20 of a chord downstream of an airfoil trailing edge. The assumption that $1/2\ \rho(v^2 + w^2)$ is negligible at Station 2 causes an additional inaccuracy, resulting in elevated drag prediction. Most experimental work attempting to predict drag by momentum defect for two-dimensional wake geometries utilize the Jones equation owing to the comparative facility of its use. No prior application of the momentum defect method has been made in the wake of a body of revolution free of sting interference effects.

Experimental Results and Analysis

The methods described in Chapter II were used to obtain a radial distribution of impact pressure 3.0 inches downstream of the ogive cylinder model. An axially symmetric wake geometry and constant free stream static pressure were assumed. Symmetry of the slip traverse data was obtained by averaging $(p_{at}-p_o)$ about the profile centerline. Simpson's composite formula for numerical integration was used in evaluating the profile drag expression (Equation A.10) in polar coordinate form.

$$D_o = 4\pi \sum_{i=0}^{n} \sqrt{p_{o_2}(r_i)-p_2(r_i)} \left\{\sqrt{p_{o_\infty}-p_\infty} - \sqrt{p_{o_2}(r_i)-p_\infty}\right\} r_i \Delta r_i \qquad (A.11)$$

As pressure data was recorded in 1/16 inch intervals during testing, the radial integration increment, Δr_i was also set at 1/16 inch. Assuming that the profile drag so calculated deviates from the profile drag indicated by the magnetic balance, the incurred error should decrease by a factor of 16 if twice as many radial intervals are used (17). A 1.6% change in C_{D_0} occurred using $\Delta r_i/2$, indicating essentially a negligible truncation error.

The probe displacement effect described in Appendix B increases the weighting function of Equation A.11, thereby increasing the magnitude of predicted profile drag. Corrections for this effect as well as for solid and wake blockage have been included in the results presented here.

As discussed in the section entitled Model Geometry and Positioning, unsteady model motion occurred primarily in the lift and slip planes while trying to maintain α_e and β_e equal to zero. Gross asymmetries resulted in the three impact pressure profiles recorded for this model orientation (for example, see Figure A-3). Referring to Table B, the calculated drag coefficient mean and standard deviation are .227 and .052 respectively for these runs. C_{D_0} as deduced from the magnetic balance currents is .196. Considering the value of standard deviation, the resulting agreement in C_{D_0} is as good as can be expected given the model position uncertainties at α_e, $\beta_e = 0$.

Three different causes of error were corrected in an effort to improve the agreement with balance force measurements.

At zero angle of attack, high rates of spin (P = 150 rps) were found to have a stabilizing effect on the model jitters. However, as would be expected, a low value of C_{D_0} (Table B) was computed from wake measurements. One source of error was assumed to be due to the effective reduction of impact pressure defect by the spin induced transverse components of velocity.

Steady non-spinning model behavior for $\alpha_e = 2$ degrees resulted in a relatively smooth distribution of impact pressure (Figure A-4). Referring to Table B, an error of 5.3% is compatible with two-dimensional results for lift coefficients greater than zero reported in the past (18). The validity of the comparison between the momentum defect and magnetic balance values of profile drag coefficient hinges on the accuracy of the location of the wake vertical centerline during testing. Thus the error caused by a slight vertical offset in a slip traverse is incorporated in the 5.3% figure as well as the above effect.

The third error source considered was variation of static pressure in the wake. This static pressure variation also sheds an interesting light on the appropriateness of the chosen probe tip position. Static pressure variation in the wake has been shown to grossly affect predicted drag error when measurements are performed close to the trailing edge of an airfoil.

Zwaaneveld (19) estimates that the drag computation performed on the basis of constant free stream static pressure (rather than the wake centerline or edge static pressures) generates the largest errors when high wake total pressure losses are measured. There has been no discussion in the literature concerning the variation of the momentum defect error, incurred by neglecting static pressure gradient, with increasing measurement distances downstream of blunt based axisymmetric bodies.

Profile drag then was therefore calculated with a static pressure distribution utilizing data measured by the static probe, Figure 6. This measured distribution is shown in Figure A-5. Turbulence was not found to be of a scale large enough to produce unsteady decreases in static pressure. The measured pressure difference (p_{at}-p) was uncertain within $\pm$ .15% q_∞ across the wake. Referring to Table B, inclusion of the static pressure gradient reduced the error in C_{D_0} by an increment of 0.5%. The static pressure variation across the wake then is seen to have only a slight effect on the profile drag coefficient predicted by momentum defect. Thus the chosen probe tip position (X/D = 3.0) is sufficiently far downstream to avoid the recirculation zone and is suggested as a guideline for the location of pressure measuring stations in similar momentum defect applications.

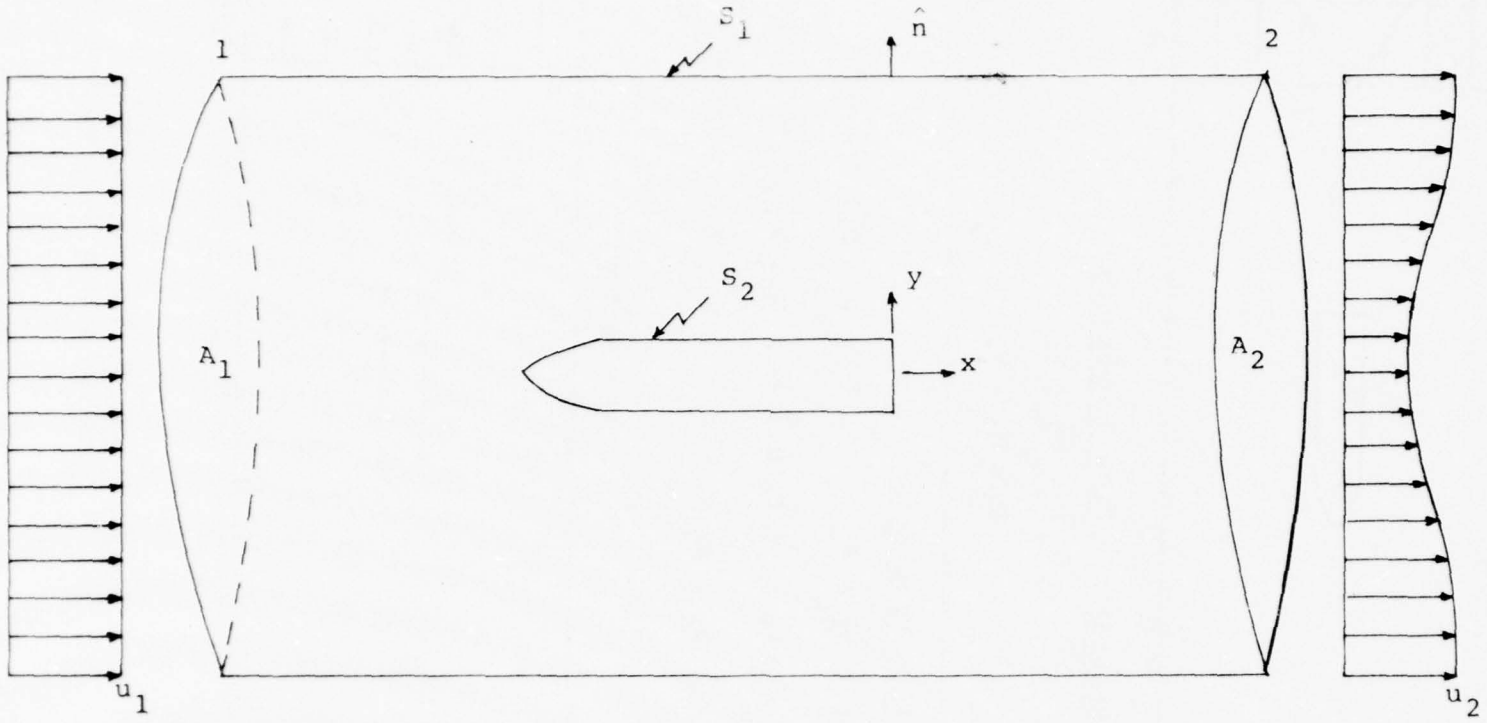

A-1 Momentum Defect Control Volume

a) Betz Method

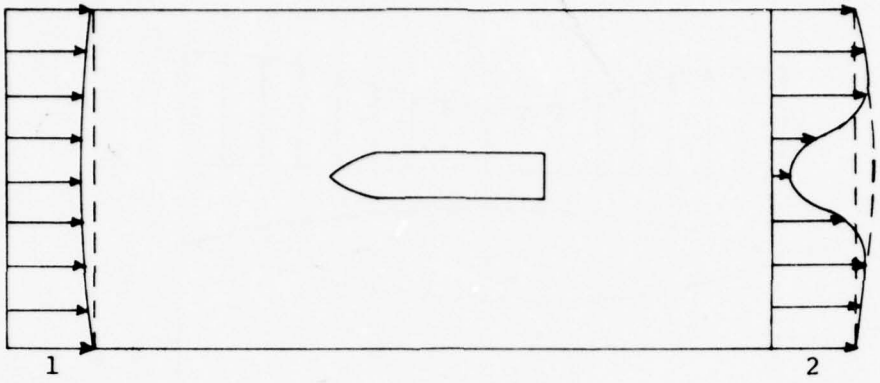

Station	Flow Properties
1	p_1, p_{o_∞}, u_1
2	p_2, p_{o_2}, u_2

Station	Flow Properties	
1	p_∞, p_{o_∞}, V_∞	$p_{o_\infty} = p_\infty + 1/2\ \rho\ V_\infty^2$
2	$p_2(r)$, $p_{o_2}(r)$, $u_2(r)$	$p_{o_2} = p_{o_3} = p_2 + 1/2\ \rho\ u_2^2$
3	p_∞, p_{o_3}, u_3	$p_{o_3} = p_\infty + 1/2\ \rho\ u_3^2$

b) Jones Method

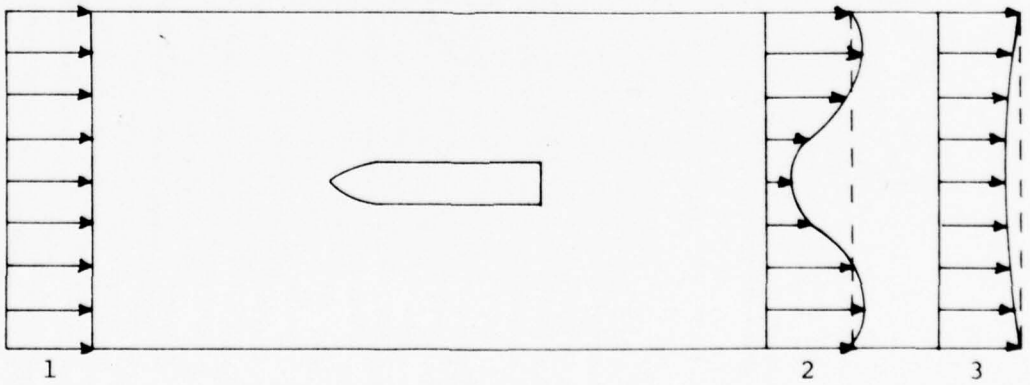

A-2 Methods for Determining
Profile Drag by Momentum Defect

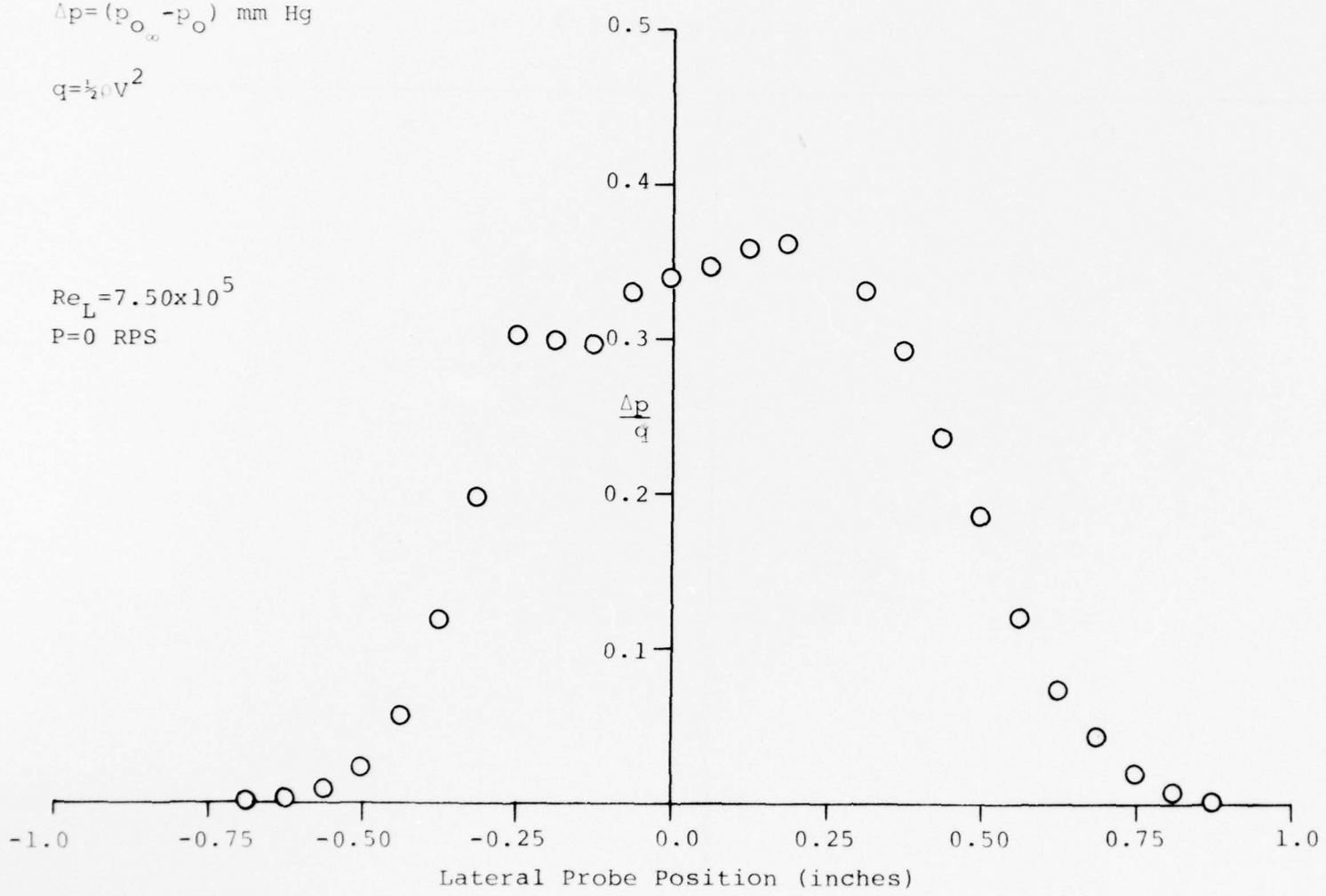

Figure A-3 Profile Asymmetry due to Model Position Uncertainty

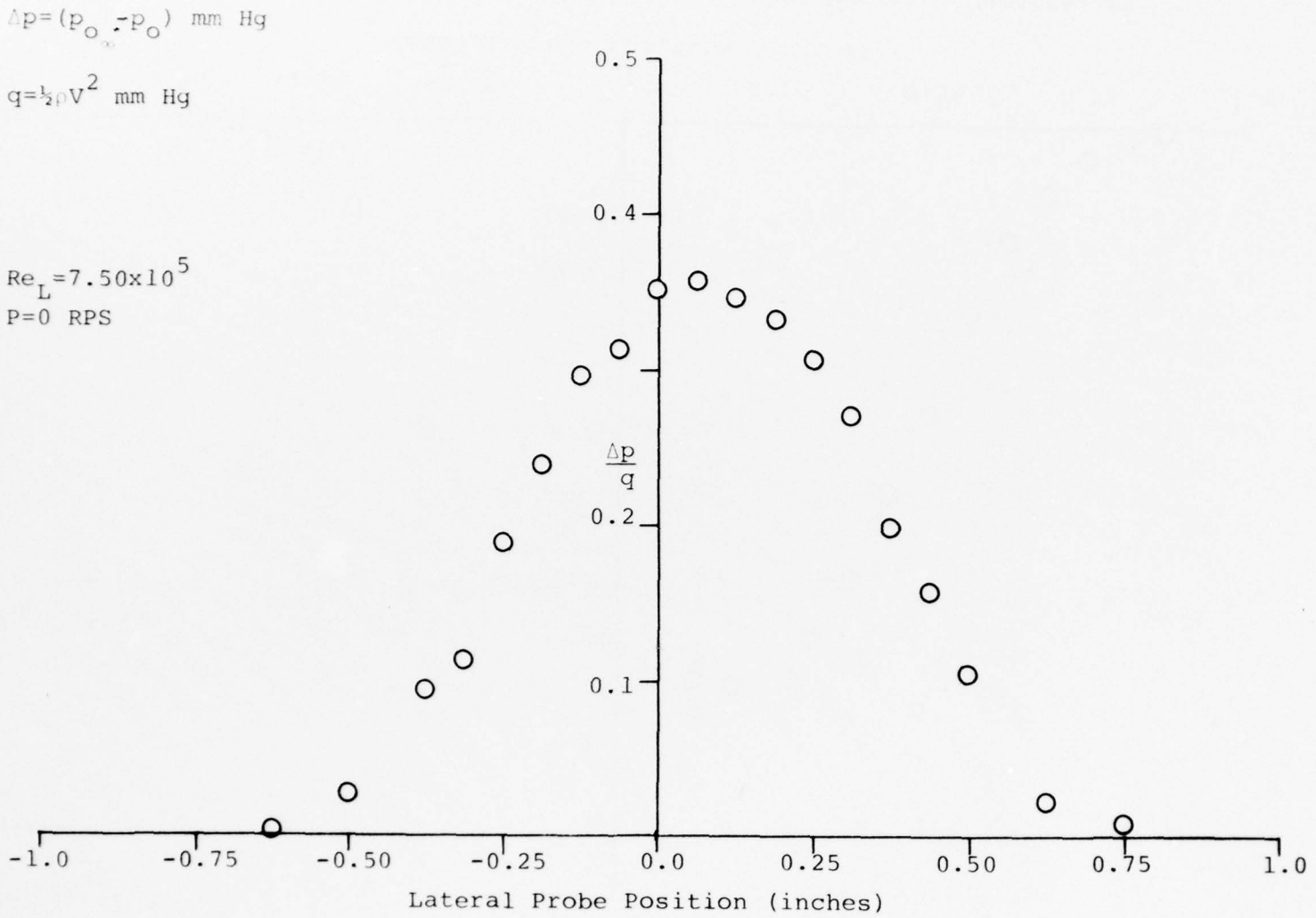

Figure A-4 Zero Spin, 2^O Momentum Defect Profile

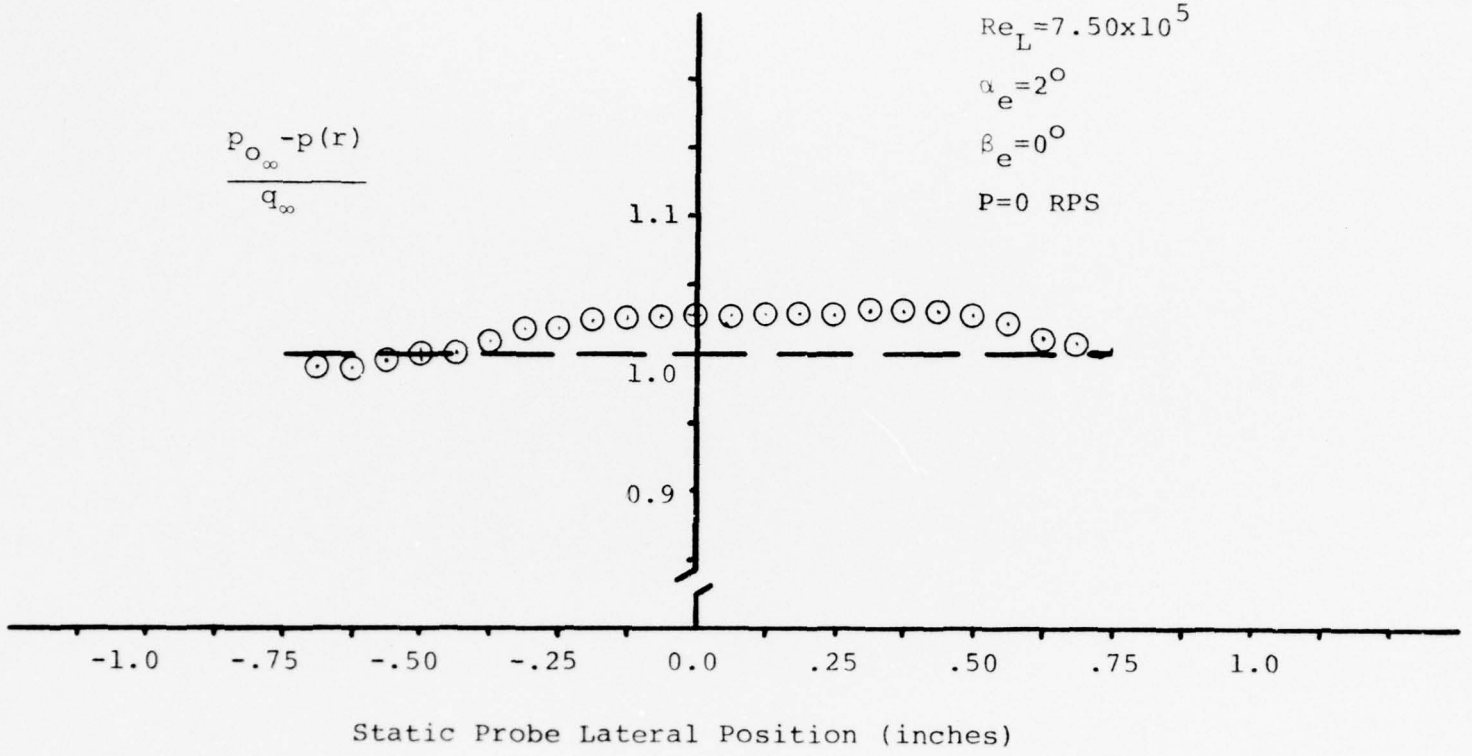

A-5 Static Pressure Distribution 3" Downstream of Model Base

Appendix B

FLOW MEASUREMENT CORRECTIONS

Displacement Effect

Impact pressure measurements are made in the wake of an ogive-cylinder. Secondary vorticity is induced in such a rotational flow with the introduction of a probe causing an effective displacement of the sensing hole center towards the region of higher total pressure. Thus, wake pressures are measured at a corrected position displaced from the true geometrical probe centerline in the direction of greater pressure. For right angle cylindrical probes, Reference 20, establishes the displacement effect correction.

$$\frac{\Delta Z}{D} = 0.13 + 0.8\,\frac{d}{D}$$

$$\Delta Z = .009 \text{ inch}$$

where D = probe O.D.

d = sensing hole I.D.

ΔZ = probe centerline displacement

The above correction is of particular importance in the measurement of profile drag by momentum defect.

Boundary Interference Effects

A model immersed in the flow of an incompressible, viscous fluid constrained by the boundaries of a closed octagonal jet experiences varying interference effects as a function of its position relative to the walls. In addition, account must be taken of buoyancy and blockage corrections which are independent of position.

Horizontal buoyancy is a continuity effect owing to boundary layer growth on the test section walls. A longitudinal static pressure gradient thus necessitates a drag force correction.

In the present case, overexpansion of the test section to accommodate turbulent boundary layer growth when in fact laminar conditions exist cause a longitudinal pressure increase tending to draw the model upstream. The buoyancy drag correction is

$$\Delta D_B = - \frac{\pi}{4} \lambda t^3 \frac{dp}{d\ell}$$

$$\Delta D_B = - 0.02 \text{ oz}$$

with λ = body shape parameter
= 4.8
t = maximum body thickness
= 1.0 inch
$\frac{dp}{d\ell}$ = longitudinal static pressure gradient
= 2.84×10^{-4} psi/inch

Presence of the model and its wake constrict the flow streamlines in a closed jet, requiring a correction in longitudinal flow quantities. A total blockage correction factor combining both solid and wake effects is estimated as follows.

$$\varepsilon_t \approx \varepsilon_S + \varepsilon_W$$

$$\approx \frac{1}{4} \frac{S}{C}$$

$$\varepsilon_t \approx .00602$$

where S = model frontal area
C = test section cross sectional area

and dynamic pressure corrected for blockage is

$$q_B \approx q_\infty (1 + 2 \varepsilon_t)$$

$$q_B \approx 1.012 \, q_\infty$$

When the model is experiencing a lift or side force, the image vortices used to model the boundaries cause a reduction of induced angle of attack and induced drag. It has been shown, Reference 21, that corrections for a circular jet, when substituted for the approximate octagonal jet corrections, admit a maximum error of 1.5% in the downwash interference parameter, δ. Thus, circular jet corrections are used here. Referring to Figure B-1, δ is a function of model translation and obeys (22).

$$\delta = \frac{1}{8\left(1-\left(\frac{d}{R}\right)^2\right)^2}$$

The correction for induced drag is given as

$$\Delta D_i = \delta q_\infty \frac{S^2}{C} C_L^2$$

Using typical lift coefficient data from Reference 9 and assuming a value of δ corresponding to a 1.0 inch model displacement, the largest correction to drag is .002 ounce (α_e = 7 degrees). As this is an order of magnitude less than the buoyancy correction, the induced drag correction is neglected.

Downwash and sidewash corrections are computed as

$$\Delta\alpha_i = \frac{w}{V_\infty} = \frac{\delta S}{C} C_L$$

$$\Delta\beta_i = \frac{v}{V_\infty} = \frac{\delta S}{C} C_Y$$

where v, w = sidewash and downwash velocities respectively.

Again basing calculations on a one-inch model displacement, typical streamline curvature corrections are shown in Table C. It can be seen that corrections to the induced angle associated with Magnus force are an order of magnitude less than the lift corrections and will be considered negligible.

In summary, then, the following boundary interference effects are applied to the test data.

$$q_B = 1.012\ q_\infty$$

$$C_D = \frac{\text{Drag}-\Delta D_B}{q_B S} + \delta \frac{S}{C} C_L^2$$

$$= \frac{\text{Drag}-.02}{q_B S}$$

and downwash angles are corrected based on the value of δ and the lift coefficient data of Reference 9.

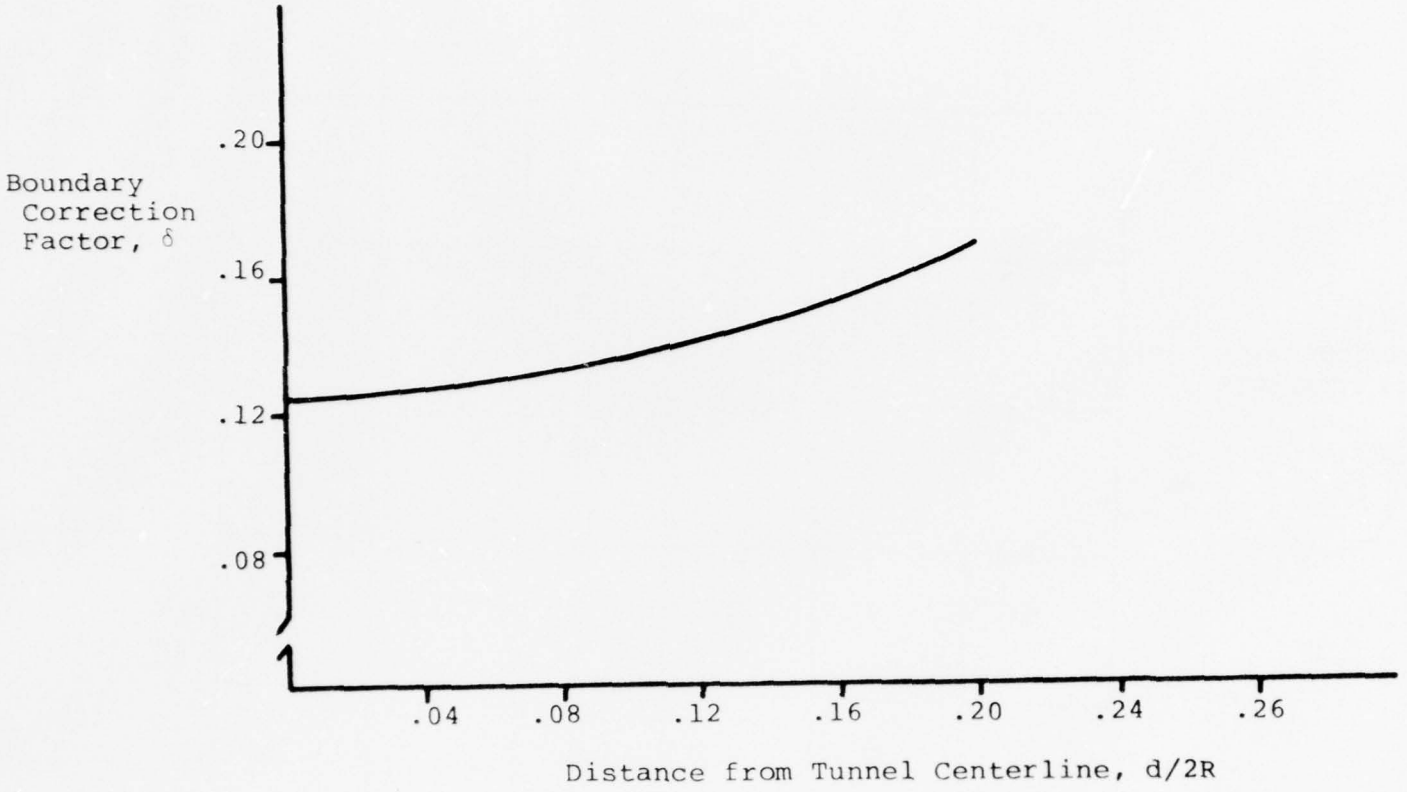
Boundary
Correction
Factor, δ
.20
.16
.12
.08
.04
.08
.12
.16
.20
.24
.26
Distance from Tunnel Centerline, d/2R

B-1 δ vs. d/2R

SPIN RATE ⇒	0 RPS		70 RPS		150 RPS	
Model Configuration	Bare	Tripped	Bare	Tripped	Bare	Tripped
α_e ⇓ $R_e \times 10^{-5}$						
0° 3.15	*£		£		£	
7.50	£	£	£	£	£	£
2° 3.15	£		£		£	
7.50	£ +.5"	£ -.5"	£ ±.5"	£ ±.5"	£ +.5"	£ ±.5"
7° 3.15	£		£		£ ±.5"	
7.50	£ ±.5"	£	£ ±.5"	£	£ ±.5"	£

* each box contains probe lift position in wake for the traverses performed

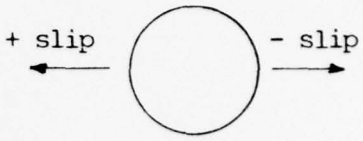

Slip Definition
View: upstream

Table A

IMPACT PRESSURE SURVEY TEST MATRIX

Table B

PROFILE DRAG RESULTS

α_e °	P(RPS)	C_{D_O} Momentum Defect	C_{D_O} Magnetic Balance
1.[1] 0	0	0.227	0.196
2. 0	150	0.156	0.196
3. 2	0	0.198	0.209
4.[2] 2	0	0.199	0.209

[1] Mean value for 3 traverses.

[2] static pressure gradient included.

Table C

DOWNWASH CORRECTIONS

$$\Delta\alpha_i = \frac{w}{V_\infty} = \frac{\delta S}{C} C_L$$

α (°)	C_L (Ref.9)	C_Y (Ref.9)	w/V_∞ (°)
7.0	0.26	-	.055
2.0	0.11	-	.023
7.0	-	-.013	-.003
2.5	-	+.013	+.003

LIST OF SYMBOLS

C_{D_0}	Profile drag coefficient = Profile drag/$q_\infty S$
C_L	Lift coefficient = Lift/$q_\infty S$
℄	Centerline position
C_Y	Side force coefficient = Side force/$q_\infty S$
D	Model base diameter (in)
D_o	Profile drag (lb)
P	Spin rate (RPS)
$PD/2V_\infty$	Non-dimensional spin parameter
p	Static pressure (mm Hg)
p_o	Impact pressure (mm Hg)
p_{at}	Ambient pressure (mm Hg)
q_∞	Free stream dynamic pressure (psi)
r	Radial distance from wake centerline (in)
Re_a	Reynolds number based on probe sensing hole radius
Re_L	Reynolds number based on model length
S	Model base area (in^2)
V_∞	Free stream velocity (ft/sec)
α_e	Effective model pitch angle
β_e	Effective model yaw angle
δ_{ij}	Kronecker delta
σ_{ij}	Stress tensor

DISTRIBUTION LIST

No. of Copies	Organization
12	Commander Defense Documentation Center ATTN: DDC-TCA Cameron Station Alexandria, VA 22314
1	Commander US Army Materiel Development and Readiness Command ATTN: DRCDMA-ST 5001 Eisenhower Avenue Alexandria, VA 22333
1	Commander US Army Aviation Systems Command ATTN: DRSAV-E 12th and Spruce Streets St. Louis, MO 63166
1	Director US Army Air Mobility Research and Development Laboratory Ames Research Center Moffett Field, CA 94035
1	Commander US Army Electronics Command ATTN: DRSEL-RD Fort Monmouth, NJ 07703
3	Commander US Army Missile Command ATTN: DRSMI-R DRSMI-RDK Mr. R. Deep Mr. R. Becht Redstone Arsenal, AL 35809
1	Commander US Army Tank Automotive Development Command ATTN: DRDTA-RWL Warren, MI 48090
2	Commander US Army Mobility Equipment Research & Development Command ATTN: Tech Docu Cen, Bldg. 315 DRSME-RZT Fort Belvoir, VA 22060
1	Commander US Army Armament Command Rock Island, IL 61202
4	Commander US Army Picatinny Arsenal ATTN: SARPA-AD Mr. S. Wasserman SARPA-FR-S-A Mr. D. Mertz Mr. E. Falkowski Mr. A. Loeb Dover, NJ 07801
2	Commander US Army Frankford Arsenal ATTN: Mr. Spencer Hirschman Mr. John Sikra Bridge and Tacony Streets Philadelphia, PA 19137
1	Commander US Army Harry Diamond Labs ATTN: DRXDO-TI 2800 Powder Mill Road Adelphi, MD 20783
1	Commander US Army Natick Research and Development Command ATTN: DRXRE, Dr. D. Sieling Natick, MA 01762
1	Director US Army TRADOC Systems Analysis Activity ATTN: ATAA-SA White Sands Missile Range NM 88002

DISTRIBUTION LIST

No. of Copies	Organization
1	Commander US Army Jefferson Proving Ground ATTN: STEJP-TD-D Madison, IN 47250
1	Commander US Army Research Office P. O. Box 12211 Research Triangle Park NC 27709
3	Commander US Naval Air Systems Command ATTN: AIR-604 Washington, DC 20360
2	Commander David W. Taylor Naval Ship Research & Development Center ATTN: Dr. S. de los Santos Mr. Stanley Gottlieb Bethesda, MD 20084
1	Commander US Naval Surface Weapons Center ATTN: Dr. T. Clare, Code DK20 Dahlgren, VA 22448
2	Commander US Naval Surface Weapons Center ATTN: Code 312, S. Hastings Code 312, F. Regan Silver Spring, MD 20910
1	Commander US Naval Weapons Center ATTN: Code 5115, Dr. A.Charters China Lake, CA 93555
1	AFATL (DLDL) Eglin AFB, FL 32542
1	Director Jet Propulsion Laboratory ATTN: Mr. B. Dayman 4800 Oak Grove Drive Pasadena, CA 91103
1	Calspan Corporation ATTN: Mr. J. Andes, Head Transonic Tunnel Dept. P. O. Box 235 Buffalo, NY 14221
1	Honeywell, Inc. ATTN: Mr. George Stilley 600 Second Street, N. Hopkins, MN 55343
1	Sandia Laboratories ATTN: Division No. 9322 Mr. Warren Curry P. O. Box 5800 Albuquerque, NM 87115
3	Massachusetts Institute of Technology ATTN: Prof. E. Covert Prof. C. Haldeman Dr. D. Finn 77 Massachusetts Avenue Cambridge, MA 02139
1	MIT/Lincoln Laboratories ATTN: Dr. Milan Vlajinac Mail Stop D-382 P. O. Box 73 Lexington, MA 02173
1	Rutgers University Mechanical, Industrial, and Aerospace Engineering Dept ATTN: Dr. Robert H. Page New Brunswick, NJ 08903

DISTRIBUTION LIST

No. of Copies	Organization
1	University of Virginia Department of Aerospace Engineering & Engineering Physics ATTN: Prof. I. Jacobson Charlottesville, VA 22904

Aberdeen Proving Ground

Marine Corps Ln Ofc
Dir, USAMSAA